J. Mech. Phys. Solids 158 (2022) 104628

Contents lists available at ScienceDirect

Journal of the Mechanics and Physics of Solids

journal homepage: www.elsevier.com/locate/jmps

Topology optimization of hard-magnetic soft materials

Zhi Zhao [a], Xiaojia Shelly Zhang [a,b,*]

[a] Department of Civil and Environmental Engineering, University of Illinois at Urbana-Champaign, 205 North Mathews Ave., Urbana, IL 61801, USA

[b] Department of Mechanical Science and Engineering, University of Illinois at Urbana-Champaign, 1206 W. Green St., Urbana, IL 61801, USA

ARTICLE INFO

Keywords:
Hard-magnetic soft materials
Topology optimization
Shape programming robots
Magnetic actuators
Programmable behaviors
Large deformations

ABSTRACT

Hard-magnetic soft materials, which consist of soft matrix embedded with hard-magnetic particles, have attracted tremendous interests owing to their untethered control capability, rapid response, and flexible programmability. This work introduces a powerful topology optimization framework to guide the rational design of hard-magnetic soft materials and structures with precisely programmable functionalities under large deformations. Built upon a unified design parameterization scheme, the proposed framework is capable of simultaneously optimizing topology, remnant magnetization distribution, and applied magnetic fields. Thus, guided by the analytical gradient information, our framework can effectively explore the entire design space to search for optimized structures with multiple target functionalities, such as programmable deformations and maximized actuation, under the corresponding optimized magnetic fields. Through five design examples, we showcase applications of the proposed framework in generating optimized shape-programming metastructures and robots, magnetic actuators, and unit cells with encoded and adaptable modes. We demonstrate how simultaneous optimization in topology, magnetization distribution, and applied magnetic field can greatly improve the performance of a design, and highlight the importance of accounting for finite-rotation kinematics to capture the influence of body torque-related magnetic force on the optimized remnant magnetization distribution. Various optimized magnetic-responsive designs with comparable performances yet distinct mechanisms are discovered, showing the effectiveness of the proposed framework to generate unconventional designs with highly programmable magnetic-actuated behaviors. We envision that the proposed topology optimization framework can potentially benefit the design process in a wide spectrum of magnetic-responsive applications, such as soft robots, magnetic actuators, and programmable metamaterials.

1. Introduction

Magnetic-responsive soft materials, allowing untethered and rapid actuation under magnetic fields, have been widely studied recently with diverse applications in the areas of robotics (Hines et al., 2017), biomedicine (Sitti, 2018), vibration mitigation (Bastola et al., 2020), etc. This work focuses on hard-magnetic soft materials (Kim et al., 2018; Zhao et al., 2019), which are obtained by embedding high-coercivity magnetic particles (e.g., neodymium–iron–boron alloy) in a soft matrix (e.g., rubber). Recently, the hard-magnetic soft materials have been shown to offer highly flexible programmability and enable various promising functionalities, such as tunable material properties (Yan et al., 2020; Chen et al., 2021; Montgomery et al., 2021) and programmable shape

* Corresponding author at: Department of Civil and Environmental Engineering, University of Illinois at Urbana-Champaign, 205 North Mathews Ave., Urbana, IL 61801, USA.

E-mail address: zhangxs@illinois.edu (X.S. Zhang).

https://doi.org/10.1016/j.jmps.2021.104628
Received 9 June 2021; Received in revised form 29 August 2021; Accepted 30 August 2021
Available online 5 September 2021
0022-5096/

transformations (Lum et al., 2016; Wang et al., 2021). Rapid developments in advanced manufacturing techniques have enabled the capability of realizing hard-magnetic soft materials with complex geometries and highly heterogeneous remnant magnetization distributions (Kim et al., 2018; Alapan et al., 2020). However, the existing design approaches for hard-magnetic soft materials have yet to fully exploit the entire design freedoms. Many impactful studies that achieve great success have adopted experience-based or bio-mimetic approaches (Kim et al., 2018; Montgomery et al., 2021; Venkiteswaran et al., 2019; Qi et al., 2020) for the considered design objectives. A few studies use optimization-based (Lum et al., 2016; Wang et al., 2021; Wu et al., 2020) and data-driven (Lloyd et al., 2020) approaches to generate designs made of hard-magnetic soft materials to achieve programmable actuation or locomotion performance, with a focus on designing the magnetization distribution of the embedded magnetic particles and/or the external magnetic fields. The design optimization of the topology or geometric features is rarely explored.

Topology optimization, as a powerful computational design tool to determine the optimal material distributions under given objective and constraint functions, holds promises to the design of stimuli-responsive materials and structures, such as piezoelectric actuation (Ruiz and Sigmund, 2018; Homayouni-Amlashi et al., 2020) and thermal action (Sigmund, 2001; Luo et al., 2009). For magnetic-responsive soft materials, Sundaram et al. (2019) use a topology optimization approach for multi-material magnetic actuators with controlled physical deflection and optical appearance. Tian et al. (2020) develop a level-set topology optimization formulation to design the matrix distribution of hard-magnetic soft materials with fixed magnetization distributions and given applied magnetic fields under the assumptions of linear elasticity. Till now, a topology optimization formulation, which is capable of simultaneously optimizing the topology (material distribution), local magnetization profile, and the external magnetic fields while capturing material nonlinearity and large-deformation kinematics, has not been established.

This work proposes a general topology optimization framework to design hard-magnetic soft materials and structures by simultaneously optimizing their topologies, remnant magnetization distributions, and the applied magnetic fields (see Fig. 1). The optimization framework is built upon the nonlinear field theory in Zhao et al. (2019) for ideal hard-magnetic soft materials. We first propose a design parameterization scheme that systematically represents the distribution of material in the matrix phase (which determines topology), the remnant magnetization distribution, and the applied magnetic field using three sets of design variables. In particular, the remnant magnetization vector at each location of the design is interpolated from a set of pre-defined candidate vectors and is promoted to converge toward one (and only one) of the candidate vectors at the end of the optimization. We then introduce a scheme to interpolate the Helmholtz free energy function from the three sets of design variables. The interpolated Helmholtz free energy function characterizes the nonlinear response of a given design under the applied magnetic field. We explore two representative design objective functions, as demonstrated in Fig. 1. The first objective is to program multiple target shapes into the design under different applied magnetic fields, and the second objective aims to maximize the actuation performance of the design at target locations. We present several numerical examples (i.e., shape-programming robots, magnetic actuators, and auxetic unit cells with different deformed modes) to showcase the capabilities of the proposed framework in designing various magnetic-responsive structures with precisely programmable functionalities. We find that the incorporation of the optimization of topology enlarges the design space and leads to designs with improved actuation performance. Additionally, the finite rotation of local magnetization vector plays an important role in determining the optimal magnetization distribution under large-deformation kinematics.

The remainder of the paper is organized as follows. Section 2 reviews the constitutive model of the nonlinear response of hard-magnetic soft materials and presents the finite element approximation of the governing equations. Section 3 introduces the proposed topology optimization framework including design parameterization, optimization formulation, and sensitivity analysis. Section 4 shows five design examples to exemplify the potential applications and demonstrate the effectiveness of the proposed framework. Section 5 contains several concluding remarks and discusses relevant future extensions of the present work. Two appendices complement the paper, which present an alternative stress constraint with corresponding designs and the effectiveness of the stress constraint.

2. Mechanics theory of hard-magnetic soft materials and finite element approximation

In this section, we briefly review the theoretical model adopted to describe the nonlinear behavior of the hard-magnetic soft materials and discuss the corresponding finite element approximation using a total Lagrangian framework. Consider a deformable solid which occupies a domain Ω in its undeformed configuration with $\boldsymbol{X}$ denoting the position vector of material particles. We assume the solid is subjected to an applied displacement field $\tilde{\boldsymbol{u}}$ on $\Gamma_{\boldsymbol{u}}$ and is traction-free on $\Gamma_{\boldsymbol{t}}$ so that $\Gamma_{\boldsymbol{u}} \cup \Gamma_{\boldsymbol{t}} = \partial\Omega$ and $\Gamma_{\boldsymbol{u}} \cap \Gamma_{\boldsymbol{t}} = \emptyset$. The solid undergoes a deformation map χ, which deforms any material particle $\boldsymbol{X}$ to the position $\boldsymbol{x} = \chi(\boldsymbol{X})$ in a deformed configuration Ω_t. The corresponding deformation gradient tensor $\boldsymbol{F}$ is given by $\boldsymbol{F} = \nabla\chi$, where ∇ stands for the gradient operator with respect to the undeformed configuration.

This work adopts the mechanics theory for ideal hard-magnetic soft materials developed by Zhao et al. (2019), which is validated to make prediction in excellent agreement with experimental results. It is worth mentioning that the theory of Zhao et al. (2019) introduces several rational assumptions to simplify what would otherwise be a complex and coupled nonlinear magneto-mechanical theory. Those assumptions include: (1) The material retains a residual magnetic flux density $\boldsymbol{B}_r$ independent of the applied magnetic field, which is much lower than the coercivity of the embedded hard-magnetic material. (2) In the undeformed configuration, the magnetic flux density $\boldsymbol{B}$ of the hard-magnetic soft material is linearly dependent on the applied magnetic field $\boldsymbol{H}$, namely, $\boldsymbol{B} = \mu_0\boldsymbol{H} + \boldsymbol{B}_r$, where $\mu_0 = 1.257\times10^{-6}$H/m is the vacuum (or air) permeability. (3) The magnetic permeability of the hard-magnetic soft material, μ_0, is the same as that of the ambient media, and the presence of the hard-magnetic soft material will not perturb the applied magnetic flux density $\boldsymbol{B}_a$. We highlight that in this study, the applied magnetic flux density is assumed to be a uniform vector.

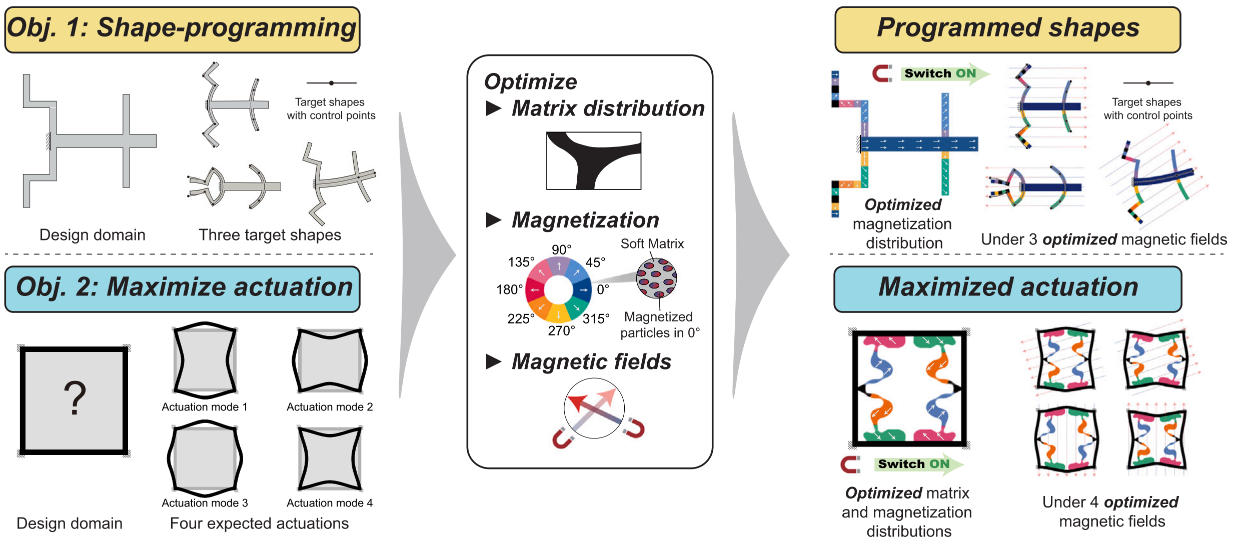

Fig. 1. Illustration of the proposed topology optimization framework for designing hard-magnetic soft materials and metastructures with two functional objectives. The objectives are to achieve shape-programming or actuation-maximized hard-magnetic soft materials by optimizing topology (matrix distribution), remnant magnetization distribution, and applied magnetic fields.

From a topology optimization perspective, the simplification in the mechanics model reduces the complexity of the computation involved in each optimization iteration. We note that for hard-magnetic soft materials with non-uniform remnant magnetization distributions, the presence of the surrounding air may have an influence on the local distributions of magnetic fields (i.e., $\boldsymbol{B}$ and $\boldsymbol{H}$) (Mukherjee et al., 2021), which will be an important future research direction.

According to the theory, the constitutive relation of the ideal hard-magnetic soft materials is described by the following nominal Helmholtz free energy function (per unit volume in the undeformed configuration) (Zhao et al., 2019):

$$W(\boldsymbol{F}, \boldsymbol{B}_r, \boldsymbol{B}_a) = W_E(\boldsymbol{F}) + W_M(\boldsymbol{F}, \boldsymbol{B}_r, \boldsymbol{B}_a) = W_E(\boldsymbol{F}) - \frac{1}{\mu_0}\boldsymbol{F}\boldsymbol{B}_r \cdot \boldsymbol{B}_a, \tag{1}$$

where $\boldsymbol{B}_r$ is the residual magnetic flux density (which relates to remnant magnetization in the undeformed configuration via $\boldsymbol{M} = \boldsymbol{B}_r/\mu_0$); $W_E(\boldsymbol{F})$ is hyperelastic stored-energy (per unit volume in the undeformed configuration) of the soft matrix materials; $W_M(\boldsymbol{F}, \boldsymbol{B}_r, \boldsymbol{B}_a) = -1/\mu_0 \boldsymbol{F}\boldsymbol{B}_r \cdot \boldsymbol{B}_a$ is magnetic free energy (per unit volume in the undeformed configuration); and $\boldsymbol{B}_a$ is the applied magnetic flux density. We note that the Helmholtz free energy is a function of the deformation gradient $\boldsymbol{F}$, and both $\boldsymbol{B}_r$ and $\boldsymbol{B}_a$ fields remain constant during the deformation process of the solid. Taking the derivative of Eq. (1) with respect to $\boldsymbol{F}$, we can obtain the first Piola–Kirchhoff stress $\boldsymbol{P}$ (Zhao et al., 2019; Dorfmann and Ogden, 2003):

$$\boldsymbol{P}(\boldsymbol{F}, \boldsymbol{B}_r, \boldsymbol{B}_a) = \frac{\partial W_E(\boldsymbol{F})}{\partial \boldsymbol{F}} - \frac{1}{\mu_0}\boldsymbol{B}_a \otimes \boldsymbol{B}_r. \tag{2}$$

The elastic part of the free energy function $W_E(\boldsymbol{F})$ can be any commonly-used hyperelastic models. In this study, we adopt the compressible Ogden model (Ogden, 1997; Feng et al., 2006) for $W_E(\boldsymbol{F})$, which is of the form:

$$W_E(\boldsymbol{F}) = \sum_{a=1}^{N_a} \frac{\mu_a}{\alpha_a}\left(\lambda_1^{\alpha_a} + \lambda_2^{\alpha_a} + \lambda_3^{\alpha_a} - 3\right) + \sum_{a=1}^{N_a} \frac{\mu_a}{\alpha_a \beta_a}\left(J^{-\alpha_a\beta_a} - 1\right), \tag{3}$$

where $\lambda_1, \lambda_2, \lambda_3$ are the principal stretches associated with the deformation gradient $\boldsymbol{F}$; $J \doteq \det(\boldsymbol{F})$; and μ_a, α_a, N_a, and β_a are material parameters such that the initial shear modulus $G = \frac{1}{2}\sum_{a=1}^{N_a} \mu_a\alpha_a$ and initial bulk modulus $\kappa = \sum_{a=1}^{N_a} \mu_a\alpha_a(\frac{1}{3} + \beta_a)$. In this work, one-term Ogden model, i.e., $N_a = 1$, is used.

In the undeformed configuration, the equilibrium of the solid is governed by:

$$\begin{aligned} &\nabla \cdot \boldsymbol{P} + \boldsymbol{b} = \boldsymbol{0} \quad \text{in} \quad \Omega, \\ &\boldsymbol{u} = \tilde{\boldsymbol{u}} \quad \text{on} \quad \Gamma_{\boldsymbol{u}}, \\ &\boldsymbol{P}\boldsymbol{N} = \boldsymbol{0} \quad \text{on} \quad \Gamma_{\boldsymbol{t}}, \end{aligned} \tag{4}$$

where $\nabla\cdot$ stands for the divergence operator in the undeformed configuration, $\boldsymbol{N}$ is the outward unit vector normal to the undeformed boundary of the solid, and $\boldsymbol{b}$ is body forces (per unit volume in the undeformed configuration), which can be neglected in this work. Introducing a virtual displacement field $\delta\boldsymbol{u}$, the variational form associated with the equilibrium Eq. (4) is obtained as

$$\int_\Omega \boldsymbol{P} : \nabla(\delta\boldsymbol{u})\mathrm{d}\boldsymbol{X} - \int_\Omega \boldsymbol{b}\cdot\delta\boldsymbol{u}\mathrm{d}\boldsymbol{X} = \boldsymbol{0}. \tag{5}$$

The above variational form is discretized using the standard bilinear quadrilateral finite elements. In the vector form, the equilibrium condition is expressed as (Zhao et al., 2019):

$$\boldsymbol{r}(\boldsymbol{u}) = \boldsymbol{f}_{\text{int}}(\boldsymbol{u}) - \boldsymbol{f}_{\text{ext}}(\boldsymbol{u}) = \boldsymbol{0}, \qquad \forall \delta \boldsymbol{u}, \tag{6}$$

where $\boldsymbol{u}$ is the displacement vector; and $\boldsymbol{r}$, $\boldsymbol{f}_{\text{int}}$ and $\boldsymbol{f}_{\text{ext}}$ are the global residual, internal force, and external force vectors, respectively. The above nonlinear system of equations is solved iteratively using the Newton–Raphson procedure with inexact line search method (Armijo, 1966; Zhang et al., 2017), which makes use of the global tangent stiffness matrix $\boldsymbol{K}_T(\boldsymbol{u}) = \partial \boldsymbol{r}/\partial \boldsymbol{u}$ evaluated according to Zhao et al. (2019). In this study, we focus on two dimensional problems under plane stress condition. Under the plane stress condition, the displacement-based finite elements are free of volumetric locking and can handle soft materials with near-incompressible behaviors (Li et al., 2021).

3. Proposed topology optimization framework

This section proposes a topology optimization framework that simultaneously optimizes 1) the matrix, 2) the remnant magnetization distributions of hard-magnetic soft materials, and 3) the external applied magnetic fields. In this section, we first introduce the design parameterization and material interpolation schemes of the proposed magnetic-responsive design framework. We then propose the optimization formulation with two representative objective functions and discuss the sensitivity analysis.

3.1. Design parameterization of hard-magnetic soft materials

We present a design parameterization scheme that simultaneously parametrizes matrix material topology, remnant magnetization distribution, and applied magnetic flux densities. Inspired by the scheme introduced in Zhang et al. (2021a), the parameterization is realized by three sets of design variables described as follows.

3.1.1. Parameterization of matrix distribution (i.e., topology)

The distribution of matrix characterizes the spatial occupancy of material. Here, a density-based approach (Bendsoe and Sigmund, 2013) is adopted. The matrix distribution is associated with the density variable $\boldsymbol{\rho}$ with ρ_e for the eth element. We apply the Heaviside projection operator (Wang et al., 2011) (with $1/2$ being its threshold) to the density variable to obtain the physical density variables $\overline{\boldsymbol{\rho}}$ with $\overline{\rho}_e$ given by

$$\overline{\rho}_e = \frac{\tanh(\frac{\beta_\rho}{2}) + \tanh(\beta_\rho(\widetilde{\rho}_e - \frac{1}{2}))}{2\tanh(\frac{\beta_\rho}{2})}, \tag{7}$$

where β_ρ being the parameter controlling the discreteness of the projection, and $\widetilde{\rho}_e$ being the intermediate design variable regularized via the density filter (Bourdin, 2001; Sigmund, 2007) as

$$\widetilde{\rho}_e = \frac{\sum_{i\in\mathcal{I}_e(R_\rho)} w_\rho^{(i,e)} v_i \rho_e}{\sum_{i\in\mathcal{I}_e(R_\rho)} w_\rho^{(i,e)} v_i}, \tag{8}$$

where $\mathcal{I}_e(R_\rho)$ is the eth element set within a prescribed region defined by a feature parameter R_ρ (e.g., a circle with a radius of R_ρ at the centroid of eth element); and v_i is the ith element volume. The weighting factor $w_\rho^{(i,e)}(R_\rho, q_\rho)$ depends on the distance between the centroids of ith and eth elements (denoted as $\boldsymbol{X}_i$ and $\boldsymbol{X}_e$, respectively), namely, $w_\rho^{(i,e)} = 1 - (\|\boldsymbol{X}_i - \boldsymbol{X}_e\|/R_\rho)^{q_\rho}$, with q_ρ being the power of the filter. The physical design variable $\overline{\rho}_e$ serves as an indicator of whether a given location in space is solid or void: $\overline{\rho}_e = 1$ represents solid and $\overline{\rho}_e = 0$ represents void.

3.1.2. Parameterization of remnant magnetization distributions

The residual magnetic flux density at each location of the design is selected from a set of N_m pre-selected candidate residual magnetic flux densities, $\boldsymbol{B}_r^{(1)}, \ldots, \boldsymbol{B}_r^{(N_m)}$, each pointing at one direction. Formally, we define the residual magnetic flux density in element e as

$$\boldsymbol{B}_{r,e} = \sum_{j=1}^{N_m} \left(\overline{m}_e^{(j)}\right)^{p_m} \boldsymbol{B}_r^{(j)}. \tag{9}$$

In the above interpolation, $\overline{m}_e^{(j)}$ is the physical magnetization variable which serves as an indicator of the magnetization of element e: $\overline{m}_e^{(j)} = 1$ means the jth candidate residual magnetic flux density $\boldsymbol{B}_r^{(j)}$ is selected, and $\overline{m}_e^{(j)} = 0$ means the jth candidate residual magnetic flux density $\boldsymbol{B}_r^{(j)}$ is not selected. A Solid Isotropic Material with Penalization (SIMP)-type (Rozvany et al., 1992; Bendsøe, 1989) penalization parameter p_m is introduced to penalize the mixture of candidate magnetizations and to promote the convergence of the physical magnetization variables to either 1 or 0.

In this work, we allow non-magnetized regions to appear in the design. Thus, the physical magnetization variables need to satisfy the following two constraints: (i) $\sum_{j=1}^{N_m} \overline{m}_e^{(j)} \leq 1$ and (ii) $\overline{m}_e^{(j)} \geq 0$, $\forall j$. We make use of the Hypercube-to-Simplex Projection (HSP) approach (Zhou et al., 2018; Zhang et al., 2021a) to define $\overline{m}_e^{(j)}$. The main advantage of HSP is that both above-mentioned constraints (i) and (ii) are satisfied implicitly by construction and, as a result, we do not need to introduce explicit constraints of $\overline{m}_e^{(j)}$ in the optimization formulation. In particular, we introduce a set of magnetization design variables $\xi_e^{(j)}$, $j = 1, \ldots, N_m$ for element e. Using the same expressions in Eqs. (7) and (8), we apply the filtering and Heaviside projection operators on the magnetization design variables to obtain intermediate variables with R_m, q_m, and β_m being filter radius, filter power, and discreteness parameter of Heaviside projection, respectively. Then, the HSP approach defines the physical magnetization variable $\overline{m}_e^{(j)}$ as

$$\overline{m}_e^{(j)} = \sum_{i=1}^{2^{N_m}} s_i^{(j)} \left((-1)^{\left(N_m + \sum_{j=1}^{N_m} c_i^{(j)}\right)} \prod_{k=1}^{N_m} \left(\overline{\xi}_e^{(k)} + c_i^{(k)} - 1 \right) \right), \tag{10}$$

where $c_i^{(j)} = \{0, 1\}$ is the ith vertex of a N_m-dimensional unit hypercube for the jth candidate remnant magnetization vector, and $s_i^{(j)}$ is the mapped vertex of a N_m-dimensional standard simplex domain:

$$s_i^{(j)} = \begin{cases} \dfrac{c_i^{(j)}}{\sum_{j=1}^{N_m} c_i^{(j)}} & \text{if } \sum_{j=1}^{N_m} c_i^{(j)} \geq 1, \\ 0 & \text{otherwise.} \end{cases} \tag{11}$$

3.1.3. Parameterization of applied magnetic flux density

Unlike the material and magnetization distributions, the applied magnetic flux density variable is assumed to be a uniform vector over the design domain. Let us consider a total of m operating conditions and denote $\boldsymbol{B}_a^{(\ell)}$ as the applied magnetic flux density in the ℓth operating condition. We express $\boldsymbol{B}_a^{(\ell)}$ as

$$\boldsymbol{B}_a^{(\ell)} = \begin{bmatrix} A_{B_a}^{(\ell)} \cos(\theta_{B_a}^{(\ell)}) \\ A_{B_a}^{(\ell)} \sin(\theta_{B_a}^{(\ell)}) \end{bmatrix}, \tag{12}$$

where $A_{B_a}^{(\ell)} \in [0, A_{\max}]$ and $\theta_{B_a}^{(\ell)} \in [0, 2\pi]$ are magnitude and angle design variables associated with the ℓth applied magnetic field, respectively.

In summary, with the three sets of physical design variables ($\overline{\boldsymbol{\rho}}$, $\overline{\boldsymbol{m}}^{(j)}$, and $\boldsymbol{B}_a^{(\ell)}$), hard-magnetic soft materials can be represented as shown in Fig. 2. The optimized matrix and remnant magnetization distributions are characterized by $\overline{\boldsymbol{\rho}}$ and $\overline{\boldsymbol{m}}^{(j)}$ (Fig. 2a), respectively. By multiplying the two physical design variables, we can obtain the optimized structure (Fig. 2b) in the undeformed configuration. Under the optimized external applied magnetic field $\boldsymbol{B}_a^{(\ell)}$, the structure achieves either shape-programming or actuation-maximized functionality (Fig. 2c), which is mainly caused by magnetic torques (induced by torques of magnetized particles essentially (Zhang et al., 2020)). We aim to obtain nearly-discrete designs (i.e., the continuous design variables $\overline{\boldsymbol{\rho}}$ and $\overline{\boldsymbol{m}}^{(j)}$ take the values close to 0 or 1), which are promoted through the Heaviside projections and the SIMP-type interpolation schemes.

3.2. Interpolation of the Helmholtz free energy function

To describe the nonlinear mechanical behavior of the hard-magnetic soft material designs, we introduce the following interpolation of the Helmholtz free energy function from the physical variables $\overline{\boldsymbol{\rho}}$ and $\overline{\boldsymbol{m}}^{(j)}$, $j = 1, \ldots, N_m$. Under the applied magnetic flux density $\boldsymbol{B}_a^{(\ell)}$, the interpolated free energy W_e of element e is given by

$$\begin{aligned} W_e(\overline{\rho}_e, \overline{m}_e^{(1)}, \ldots, \overline{m}_e^{(N_m)}, \boldsymbol{B}_a^{(\ell)}, \boldsymbol{u}_e^{(\ell)}) = &\left[\epsilon + (1-\epsilon)(\overline{\rho}_e)^{p_\rho}\right] W_E(\boldsymbol{u}_e^{(\ell)}) + \\ &(\overline{\rho}_e)^{p_\rho} W_M\left(\boldsymbol{u}_e^{(\ell)}, \boldsymbol{B}_{r,e}(\overline{m}_e^{(1)}, \ldots, \overline{m}_e^{(N_m)}), \boldsymbol{B}_a^{(\ell)}\right), \end{aligned} \tag{13}$$

where $\boldsymbol{u}_e^{(\ell)}$ is the displacement vector in element e under $\boldsymbol{B}_a^{(\ell)}$; and $\epsilon = 10^{-5}$ is a small value to avoid singular stiffness. In the above interpolation formula, the SIMP approach (Bendsoe and Sigmund, 2013; Bendsøe, 1989) is used to penalize both elastic-stored energy and magnetic free energy associated with intermediate variables of $\overline{\rho}_e$ to drive them toward either 0 or 1. The penalization parameters associated with both energies are taken to be the same, which is found to alleviate the parasite effect commonly found in topology optimization considering design-dependent loads (Ruiz and Sigmund, 2018; Bruyneel and Duysinx, 2005; Zhang et al., 2021b). In addition, based on our numerical experience, excessive deformations of low-stiffness regions can lead to numerical instabilities in FE analysis during the optimization. Thus, the energy interpolation scheme (Wang et al., 2014) is applied to the stored-energy W_E to address the numerical instabilities of low stiffness regions (defined to be regions with $(\overline{\rho}_e)^{p_\rho} \leq 0.01$ in this work). We also apply the same concept to the magnetic free energy W_M so that the magnetic actuation in low stiffness regions is negligible. The readers are referred to Wang et al. (2014) for details.

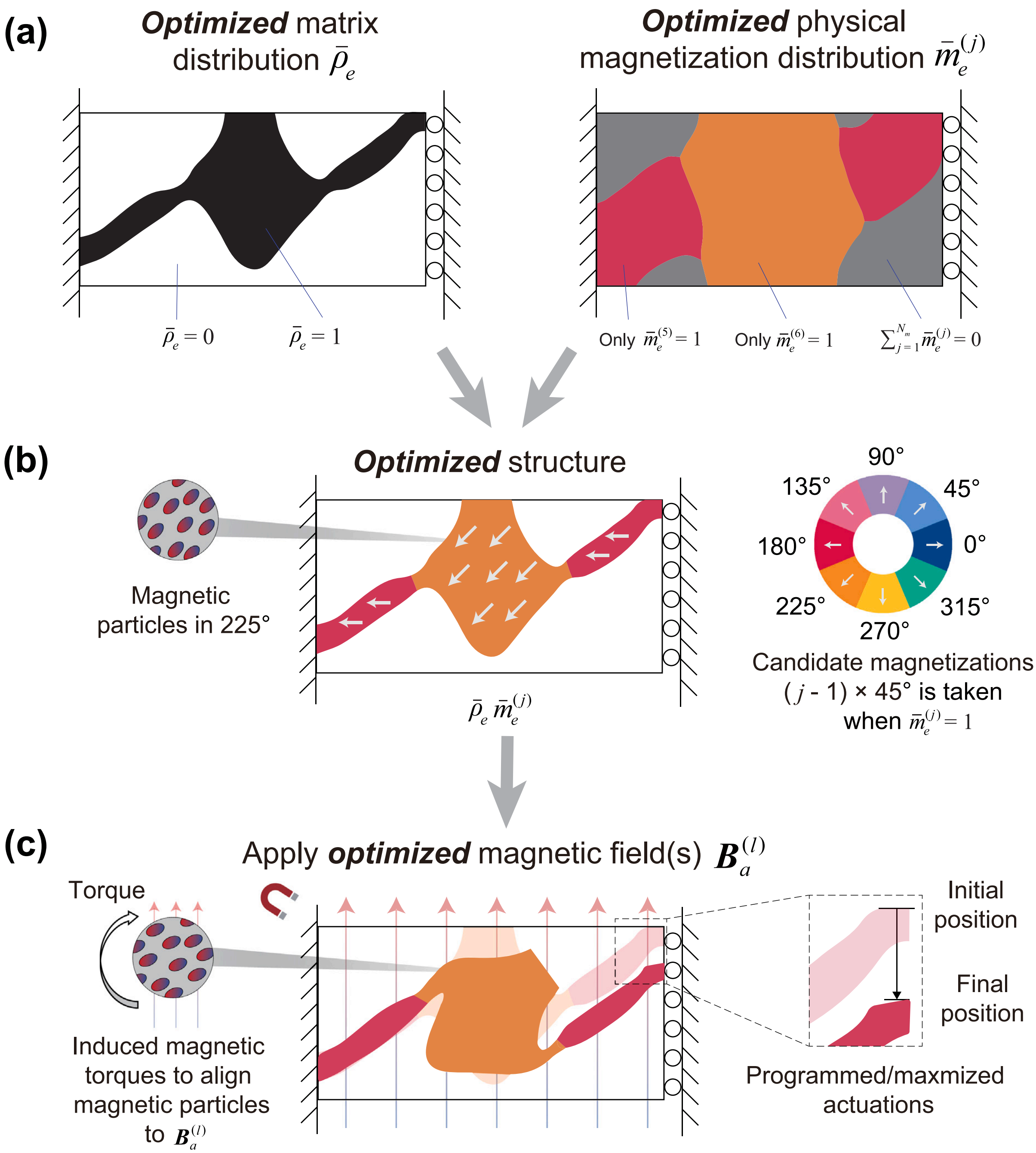

Fig. 2. Illustration of an optimized magnetic-responsive design represented by three sets of physical design variables ($\bar{\boldsymbol{\rho}}$, $\bar{\boldsymbol{m}}$, and $\boldsymbol{B}_a^{(l)}$): (a) Matrix and remnant magnetization distributions represented by $\bar{\boldsymbol{\rho}}$ and $\bar{\boldsymbol{m}}$, respectively; (b) Optimized design by multiplying $\bar{\boldsymbol{\rho}}$ and $\bar{\boldsymbol{m}}$; (c) Deformation mechanism under optimized magnetic field $\boldsymbol{B}_a^{(l)}$.

3.3. Optimization formulation

Having introduced the design parameterization and free-energy interpolation schemes, we now propose the topology optimization formulation to generate optimized designs composed of hard-magnetic soft materials. Let us assume that there is a total of N_ℓ of applied magnetic fields, denoted as $\boldsymbol{B}_a^{(1)}, \ldots, \boldsymbol{B}_a^{(N_\ell)}$, which can be either optimized (treated as design variables) or pre-determined. The mesh Ω_h is composed of N_e elements and N_n nodes. The goal of the proposed topology optimization is to minimize a certain performance objective $f(\cdot)$ which collects the nonlinear responses (represented by the displacement vectors $\boldsymbol{u}^{(1)}, \ldots, \boldsymbol{u}^{(\ell)}$) of the design under those applied magnetic fields.

Formally, we formulate the topology optimization problem as:

$$\begin{aligned}
\min_{\substack{\rho,\xi^{(1)},\ldots,\xi^{(N_m)},\\ \boldsymbol{B}_a^{(1)},\ldots,\boldsymbol{B}_a^{(N_\ell)}}} \quad & f\left(\boldsymbol{u}^{(1)}, \ldots, \boldsymbol{u}^{(N_\ell)}\right) \\
\text{s.t.:} \quad & \frac{\boldsymbol{v}^T\overline{\boldsymbol{\rho}}}{|\Omega_h|} \leq v_{\max} \\
& \left\{\sum_{e=1}^{N_e}\left[\frac{w_\sigma(\overline{\rho}_e)}{v_e}\int_{\Omega_{h,e}}\sigma_{\mathrm{VM}}\left(\boldsymbol{\sigma}_E\left(\boldsymbol{u}^{(\ell)}\right)\right)\mathrm{d}\boldsymbol{X}\right]^{p_n}\right\}^{1/p_n} \leq \sigma_{\max}^{(\ell)}, \quad \ell = 1, \ldots, N_\ell \\
& \boldsymbol{r}(\overline{\boldsymbol{\rho}}, \overline{\boldsymbol{m}}^{(1)}, \ldots, \overline{\boldsymbol{m}}^{(N_m)}, \boldsymbol{B}_a^{(\ell)}, \boldsymbol{u}^{(\ell)}) = \boldsymbol{0}, \quad \ell = 1, \ldots, N_\ell \\
& \boldsymbol{0} \leq \boldsymbol{\rho} \leq \boldsymbol{1} \\
& \boldsymbol{0} \leq \boldsymbol{\xi}^{(j)} \leq \boldsymbol{1}, \quad j = 1, \ldots, N_m \\
& 0 \leq A_{B_a}^{(\ell)} \leq A_{\max}, \quad \ell = 1, \ldots, N_\ell \\
& 0 \leq \theta_{B_a}^{(\ell)} \leq 2\pi, \quad \ell = 1, \ldots, N_\ell,
\end{aligned} \tag{14}$$

where $\boldsymbol{v}$ is the element volume vector with v_e being the volume of element e; $v_{\max}$ is the assigned maximum volume for matrix materials. We note that the above formulation allows the three sets of design variables ($\boldsymbol{\rho}$, $\boldsymbol{\xi}^{(j)}$, and $\boldsymbol{B}_a^{(\ell)}$) to be optimized either simultaneously or selectively. For example, if one wants to only optimize the matrix material topology under the prescribed remnant magnetization distribution and applied magnetic fields, then one can fix the design variables $\boldsymbol{\xi}^{(j)}$ and $\boldsymbol{B}_a^{(\ell)}$ throughout the optimization and only optimize the design variable $\boldsymbol{\rho}$.

In addition, the above optimization formulation incorporates stress constraints in which the von-Mise stress $\sigma_{\mathrm{VM}}(\cdot)$ associated with the Cauchy stress tensor of elastic stored-energy $\boldsymbol{\sigma}_E = 1/J(\partial W_E(\boldsymbol{F})/\partial \boldsymbol{F})\boldsymbol{F}^T$ (i.e., mechanical Cauchy stress) is constrained to be below a prescribed upper bound. Notably, the mechanical Cauchy stress is symmetric and only explicitly depends on the density variable $\boldsymbol{\rho}$ and displacement vector $\boldsymbol{u}^{(\ell)}$. Alternatively, the stress constraint can be imposed on the total Cauchy stress, which is an asymmetric tensor (Zhao et al., 2019) and depends on additional design variables $\boldsymbol{\xi}$ and $\boldsymbol{B}_a$. This alternative total Cauchy stress constraint and the comparison with the mechanical Cauchy stress are reported in Appendix A. The stress constraint is imposed individually on the deformation state $\boldsymbol{u}^{(\ell)}$ under each applied magnetic flux density $\boldsymbol{B}_a^{(\ell)}$ with $\sigma_{\max}^{(\ell)}$ being a user-defined upper bound. To prevent the singularity issue in the stress constrained topology optimization (Cheng and Jiang, 1992; Duysinx and Bendsøe, 1998; Bruggi, 2008), we adopt the relaxation approach proposed by Bruggi (2008) and define $w_\sigma(\overline{\rho}_e) \doteq \epsilon + (1-\epsilon)\overline{\rho}_e^{-q_\rho}$ with q_ρ chosen as $q_\rho = 1/3$. The stress constraint is handled by the p-norm approach (Duysinx and Bendsøe, 1998) with $p_n = 12$. We note that the stress constraint serves as a numerical technique, which is found to be effective in this study, to prevent thin members and hinge-like connections from appearing in the optimized design as well as to limit the level of local deformations (Li et al., 2021) (see Appendix B for the demonstration of effectiveness). They are not related to the physical material failure of hard-magnetic soft materials.

This study considers two representative performance objective functions $f(\cdot)$. One aims to program a set of target deformation shapes into the design, which may be useful for robotic applications. The other maximizes the deformation of the design at several target locations, which can be employed in design devices such as actuators. The first objective function is defined as

$$f_1(\boldsymbol{u}^{(1)}, \ldots, \boldsymbol{u}^{(N_\ell)}) = \max_{\ell\in\{1,\ldots,N_\ell\}}\left(\frac{1}{N_\alpha}\sum_{\alpha=1}^{N_\alpha}\left(u_\alpha^{(\ell)} - u_\alpha^{*(\ell)}\right)^2\right), \tag{15}$$

where $u_\alpha^{(\ell)}$ and $u_\alpha^{*(\ell)}$ are respectively the actual and target displacements at αth control degree of freedom (DOF) under $\boldsymbol{B}_a^{(\ell)}$ in the ℓth operating condition; and N_α is the total number of selected control DOFs. This objective function aims to minimize the maximum mean square error of the actual and target displacements at the control points under a set of (optimized or pre-defined) applied magnetic fields. The second objective function is defined as

$$f_2(\boldsymbol{u}^{(1)}, \ldots, \boldsymbol{u}^{(N_\ell)}) = \max_{\substack{\ell\in\{1,\ldots,N_\ell\}\\ \alpha\in\{1,\ldots,N_\alpha^{(\ell)}\}}} u_\alpha^{(\ell)}, \tag{16}$$

where $u_\alpha^{(\ell)}$ is the actual displacement at the αth control DOF under $\boldsymbol{B}_a^{(\ell)}$; and N_α is the total number of selected control DOFs. We note that the actual displacement $u_\alpha^{(\ell)}$ is defined to take appropriate sign so that minimizing $u_\alpha^{(\ell)}$ equals to maximizing it in the opposite direction (which is the target direction).

The proposed formulation (14) is solved by gradient-based update algorithm. Thus, the sensitivities information of objective and constraint functions with respect to the design variables are required. We use the adjoint method (Bendsoe and Sigmund, 2013) to perform the sensitivity analysis. For simplicity, we use a generic function ϕ to represent either an objective or a constraint function. The sensitivity of ϕ with respect to the physical variables $\overline{\boldsymbol{\rho}}$ and $\overline{\boldsymbol{m}}^{(j)}, j = 1, \ldots, N_m$ are given by

$$\frac{\partial\phi}{\partial\overline{\rho}_e} = \frac{\partial\phi\left(\overline{\boldsymbol{\rho}}, \overline{\boldsymbol{m}}^{(1)}, \ldots, \overline{\boldsymbol{m}}^{(N_m)}, \boldsymbol{B}_a^{(\ell)}, \boldsymbol{u}^{(\ell)}\right)}{\partial\overline{\rho}_e} + (\lambda^{(\ell)})^T\frac{\partial\boldsymbol{r}\left(\overline{\boldsymbol{\rho}}, \overline{\boldsymbol{m}}^{(1)}, \ldots, \overline{\boldsymbol{m}}^{(N_m)}, \boldsymbol{B}_a^{(\ell)}, \boldsymbol{u}^{(\ell)}\right)}{\partial\overline{\rho}_e}, \tag{17}$$

Table 1
Brief description of the numerical examples.

Ex.	Name	Design variables	Obj. function	Feature
1	Shape-programming arm	ξ and $\boldsymbol{B}_a$	$f_1(\cdot)$	Enable a shape-programming arm achieving 5 target shapes under corresponding optimized magnetic fields
2	Frog-inspired swimming robot	ξ and $\boldsymbol{B}_a$	$f_1(\cdot)$	Program 3 motions (thrust, insweep, and steering phases) in a frog-inspired swimming robot under corresponding optimized magnetic fields
3	Magnetic-responsive double-clamped actuator	ρ and ξ	$f_2(\cdot)$	Demonstrate the importance and advantage of incorporating matrix optimization; Investigate the influences of design parameters on optimized results
4	Magnetic actuator with local magnetization regions	ρ and ξ	$f_2(\cdot)$	Study a variety of magnetic actuators generated by assigning different local magnetization zones
5	Magnetic-responsive unit cell design	ρ, ξ, and $\boldsymbol{B}_a$	$f_2(\cdot)$	Discover multiple magnetic-responsive unit cells achieving various programmed actuation modes under different magnetic fields

and

$$\frac{\partial \phi}{\partial \overline{m}_e^{(j)}} = \frac{\partial \phi\left(\overline{\rho}, \overline{\boldsymbol{m}}^{(1)}, \ldots, \overline{\boldsymbol{m}}^{(N_m)}, \boldsymbol{B}_a^{(\ell)}, \boldsymbol{u}^{(\ell)}\right)}{\overline{m}_e^{(j)}} + (\lambda^{(\ell)})^T \frac{\partial \boldsymbol{r}\left(\overline{\rho}, \overline{\boldsymbol{m}}^{(1)}, \ldots, \overline{\boldsymbol{m}}^{(N_m)}, \boldsymbol{B}_a^{(\ell)}, \boldsymbol{u}^{(\ell)}\right)}{\partial \overline{m}_e^{(j)}}, \quad j = 1, \ldots, N_m, \tag{18}$$

respectively, where $\lambda^{(\ell)}$ is the adjoint vector obtained from solving the following adjoint equation associated with the ℓth magnetic field:

$$\left[\boldsymbol{K}_T^{(\ell)}(\overline{\rho}, \overline{\boldsymbol{m}}^{(1)}, \ldots, \overline{\boldsymbol{m}}^{(N_m)}, \boldsymbol{B}_a^{(\ell)}, \boldsymbol{u}^{(\ell)})\right] \lambda^{(\ell)} = -\frac{\partial \phi\left(\overline{\rho}, \overline{\boldsymbol{m}}^{(1)}, \ldots, \overline{\boldsymbol{m}}^{(N_m)}, \boldsymbol{B}_a^{(\ell)}, \boldsymbol{u}^{(\ell)}\right)}{\partial \boldsymbol{u}^{(\ell)}}, \tag{19}$$

with $\boldsymbol{K}_T^{(\ell)}$ being the tangent stiffness matrix associated with $\boldsymbol{B}_a^{(\ell)}$. Once the sensitivities $\partial\phi/\partial\overline{\rho}_e$ and $\partial\phi/\partial\overline{m}_e^{(j)}$ are obtained, the sensitivities of ϕ with respect to the design variables ρ and $\xi^{(j)}$ can be obtained through differentiating expressions (Eqs. (7), (8), and (10)) and using the chain rule (Bruns and Tortorelli, 2001; Wang et al., 2011). The sensitivity of ϕ with respect to the design variables $A_{B_a}^{(\ell)}$ and $\theta_{B_a}^{(\ell)}$ associated with $\boldsymbol{B}_a^{(\ell)}$ can be obtained using the same procedure as Eqs. (17) and (18). The method of moving asymptotes (MMA) (Svanberg, 1987) is adopted together with the bound formulation (Olhoff, 1989) to handle the min–max type objective functions (Eqs. (15) and (16)).

4. Numerical examples

This section presents five examples to demonstrate the capability of the proposed framework in optimizing designs composed of hard-magnetic soft materials, which are summarized in Table 1. Examples 1 and 2 aim to program a set of target deformed shapes into an arm and a swimming robot by simultaneously optimizing their remnant magnetization distribution and the applied magnetic fields. Example 3 maximizes the performance of a magnetic actuator by simultaneously optimizing the topology (i.e. distribution of matrix materials) and remnant magnetization distributions. This example also showcases the improved performance enabled by optimizing the topology and investigates the influences of various design parameters on the optimized designs, actuation performances, and corresponding mechanisms. Example 4 designs magnetic actuators by simultaneously optimizing their topologies and remnant magnetization distributions. This example shows that assigning different active magnetization zones in the design domain leads to optimized actuators with distinct actuation mechanisms yet comparable performances. Example 5 generates unit cells that achieve different actuation modes under various applied magnetic fields (which mimic materials with positive and negative Poisson's ratios) by simultaneously optimizing topology, remnant magnetization distributions, and the applied magnetic fields. The last example also studies how various initial guesses influence the discovered designs as well as their actuation mechanisms. The objective function $f_1(\cdot)$ (Eq. (15)) is applied to Examples 1 and 2 and the objective function $f_2(\cdot)$ (Eq. (16)) is employed in Examples 3–5. The adopted matrix material properties in all the examples are selected based on the measured experimental data (Zhao et al., 2019; Poulain et al., 2017) of silicon-based elastomers. The specific values of material properties in the examples are tuned to avoid excessive deformations and convergence difficulties of FE analysis during the optimization.

In terms of the topology optimization setup, we apply the continuation strategy to penalization parameters p_ρ and p_m (in Eqs. (13) and (9), respectively) as well as the sharpness parameters β_ρ and β_m associated with the Heaviside projection. We first simultaneously increase p_ρ and p_m (e.g., $p_\rho = p_m = 1, 1.5, \ldots, 3$), following by sequentially doubling β_m (e.g., $\beta_m = 1, 2, 4, \ldots, 32$) and then β_ρ (e.g., $\beta_\rho = 1, 2, 4, \ldots, 32$) until well-defined results are obtained. A further illustration of the parameter continuation strategy is discussed based on a representative case in Section 4.3.

4.1. Shape programming robots under magnetic actuation

This subsection focuses on the generation of metastructures with programmed shapes, which is a popular design problem for many soft robotic applications (see, for example, Lum et al., 2016; Wang et al., 2021). More specifically, our goal is to program a set of target deformed shapes into a magnetic-responsive metastructure by optimizing both the remnant magnetization distribution and the corresponding set of applied magnetic fields, with each field induces one target deformed shape. We introduce two design problems to demonstrate the capabilities of the proposed framework to generate shape-programming magnetic-responsive metastructures.

4.1.1. Example 1: Shape-programming arm

In this design problem, we aim to achieve a shape-programming arm by optimizing remnant magnetization distribution and applied magnetic fields. The dimension of the design domain is shown in Fig. 3(a). The domain is discretized by $400 \times 10 = 4,000$ quadrilateral finite elements. As demonstrated by the solid lines with markers in Fig. 3(c), we prescribe $N_\ell = 5$ target shapes by assigning the corresponding target displacements (in both x and y directions) to the 10 (corresponds to $N_\alpha^{(1,2,\ldots,N_\ell)} = 20$) uniformly-distributed control points along the center line of the arm. The matrix material is modeled by the compressible Ogden model with $\mu_a = 1$ MPa, $\alpha_a = 2$, and $\beta_a = 24.5$, which lead to $G = 1$MPa and $\kappa = 50$MPa. There are a total of $N_m = 8$ candidate magnetization vectors, $\boldsymbol{B}_r^{(j)}$, $j = 1, \ldots, 8$, whose orientations are 45° apart from each other and magnitudes are all equal to 100mT. In addition to these candidate magnetization vectors, non-magnetized regions are also allowed at each location of the optimized design. To ensure the remnant magnetization is uniform within each 2mm by 4mm sub-region in Fig. 3(a), we set $q_m = 0$ and $R_m = 4$mm as the length of each sub-region. The number of candidate magnetization vectors and the size of the sub-region (i.e., the programming resolution of remnant magnetization) are selected for a demonstration purpose, and they are adjustable to comply with the requirements of selected manufacturing approaches. In addition, maximum magnitude of the applied magnetic field $A_{\max}$ is set as 30mT. The optimization starts from an initial design with solid material $\boldsymbol{\rho} = \mathbf{1}$ and uniform magnetization (namely, $\xi_e^{(j)} = 1/8$). The initial applied magnetic fields are taken as $\boldsymbol{B}_a^{(\ell)} = [0, -A_{\max}/2]$mT, $\forall \ell \in \{1, \ldots, 5\}$. During the optimization, the density design variables $\boldsymbol{\rho}$ are kept constant as we gradually optimize the design variables $\boldsymbol{\xi}^{(j)}$ and $\boldsymbol{B}_a^{(\ell)}$ to minimize the objective function value. Because the matrix materials are treated as non-designable in this example, the volume and stress constraints in the optimization formulation (14) are inactive accordingly.

The optimized remnant magnetization distribution, the five optimized applied magnetic fields, and the corresponding five deformed shapes are shown in Fig. 3(b)–(c). Both magnetized and non-magnetized regions exist in the optimized design, suggesting that the entire domain does not need to be magnetized to achieve the five target shapes. To quantify the fitting error, we define the following error measure:

$$\text{Error} = \max_{\ell \in \{1,\ldots,N_\ell\}} \left[\frac{1}{N_\alpha^{(\ell)}} \sum_{\alpha=1}^{N_\alpha^{(\ell)}} \left| \frac{u_\alpha^{(\ell)} - u_\alpha^{*(\ell)}}{u_\alpha^{*(\ell)}} \right| \right], \tag{20}$$

where $|\cdot|$ stands for the absolute operator. This error is measured to be 0.12% for the obtained optimized design, suggesting that the arm with optimized remnant magnetization distribution deforms precisely to the five target shapes when subjected to each of the five corresponding optimized applied magnetic fields.

4.1.2. Example 2: Frog-inspired swimming robot

A frog-inspired swimming robot design with optimized remnant magnetization distribution and optimized magnetic fields is presented in this subsection to further demonstrate the capability of generating shape-programming metastructures. The dimension of the design domain is shown in Fig. 4(a) with a FE mesh of 7000 quadrilateral elements. As demonstrated by the solid lines with markers in Fig. 4(c), we prescribe $N_\ell = 3$ target shapes, i.e., thrust, insweep, and steering phases, by assigning the corresponding target displacements (in both x and y directions) to 10, 10, and 2 control points (corresponding to $N_\alpha^{(1)} = 20$, $N_\alpha^{(2)} = 20$, and $N_\alpha^{(3)} = 4$), respectively. The matrix material is characterized by the compressible Ogden model with $\mu_a = 0.33$MPa, $\alpha_a = 2$, and $\beta_a = 24.5$, which lead to $G = 0.33$MPa and $\kappa = 16.67$MPa. There are a total of $N_m = 8$ candidate magnetization vectors, $\boldsymbol{B}_r^{(j)}$, $j = 1, \ldots, 8$, whose orientations are 45° apart from each other and magnitudes are all equal to 100mT. In addition to these candidate magnetization vectors, non-magnetized regions are also allowed at each location of the optimized design. To ensure the remnant magnetization is uniform within each 2mm by 2mm square in Fig. 4(a), we set $R_m = 2$mm as the length of each sub-region. In addition, the maximum magnitude of the applied magnetic field $A_{\max}$ is set as 50mT. To enable symmetric deformations with respect to the x direction for target shapes 1 and 2, we fix the directions of the associated applied magnetic fields ($\boldsymbol{B}_a^{(1)}$ and $\boldsymbol{B}_a^{(2)}$) towards the left and right, respectively, and set the residual magnetization of the central rectangular region (32mm*4mm) to be a constant vector, which has the magnitude of 100mT and points rightward. The initial guesses of design variables and optimization setup are the same as the ones we describe in Section 4.1.1.

Fig. 4(b)–(c) show the frog-inspired swimming robot design including the optimized remnant magnetization distribution, the three optimized magnetic fields, and the corresponding three deformed shapes. The obtained remnant magnetization distribution (Fig. 4b) is non-intuitive owing to the relatively complex prescribed topology and target shapes. As shown in Fig. 4(c), the actuation shapes 1 and 2 under the two opposite horizontal magnetic fields can guide the motions of the swimming robot in the thrust and insweep phases, respectively, driving it to move forward. The tilted magnetic field steers the swimming robot to change its direction, as demonstrated in the actuation shape 3. The error (quantified by Eq. (20)) between the actual and target shapes is 16%, which is

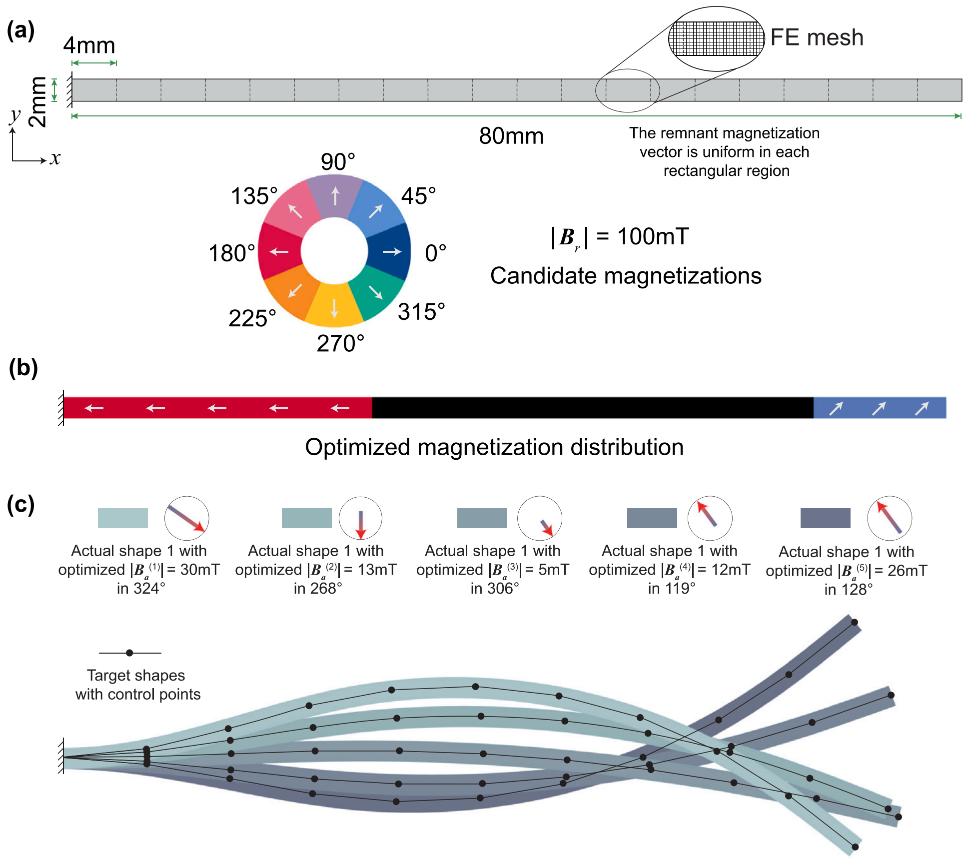

Fig. 3. Shape-programming arm: (a) Design domain and candidate magnetizations; (b) Optimized remnant magnetization distribution; (c) Target and optimized actual shapes (0.12% error).

larger than the design shown in Section 4.1.1 owing to the increased complexity of this design problem. Having encoded those three basic quasi-static motions (i.e., thrust, insweep, and steering phases), the frog-inspired swimming robot is promising to be used for a robotic application to complete sophisticated tasks.

In summary, both designs presented in this subsection showcase the effectiveness of the proposed topology optimization approach in generating accurate shape-programming designs under a number of optimized applied magnetic fields. This capability of the proposed framework makes it a promising design tool to encode various quasi-static motions into magnetic-responsive soft robots, for example, by sequentially varying the applied magnetic fields, to generate complex locomotion (Lum et al., 2016; Wu et al., 2020).

4.2. Example 3: Magnetic-responsive double-clamped actuator with maximized actuation performance

Example 3 aims to highlight the importance and advantage of optimizing matrix topology in the proposed framework by demonstrating that simultaneously optimizing both matrix topology and remnant magnetization distribution can lead to designs with improved performance as compared to optimizing the remnant magnetization distribution alone. In addition, this example also investigates the influences of several design parameters on the optimized designs and corresponding mechanisms.

We consider a double-clamped rectangular design region with its dimensions and boundary conditions shown in Fig. 5(a). The domain is discretized by $300 \times 75 = 22,500$ quadrilateral finite elements. To model the feedback force of the actuator, we connect springs to center nodes on the top of the design domain (Bendsoe and Sigmund, 2013; Zhu et al., 2020). Each spring has a constant stiffness which are summed to be k_{out}. A larger k_{out} leads to a larger actuation force generated by the optimized actuator. These connected center nodes are also taken as the control points (i.e., $N_{\alpha}^{(1,2,\ldots,N_{\ell})} = 5$) and we aim to minimize their upward displacements (which correspond to maximizing the displacement in the downward direction) using objective function $f_2(\cdot)$ in Eq. (16) with $N_{\ell} = 1$. To compare the final performance of the optimized designs, we report the averaged value of the downward displacement in those control points, denoted as $\bar{u}_{\text{out}}$. A larger $\bar{u}_{\text{out}}$ value indicates better actuation performance.

The matrix material is modeled by the compressible Ogden model with $\mu_a = 0.33$ MPa, $\alpha_a = 2$, and $\beta_a = 499.5$, leading to $G = 0.33$MPa and $\kappa = 333$MPa. We consider a total of $N_m = 8$ candidate magnetization vectors with uniform orientation space of

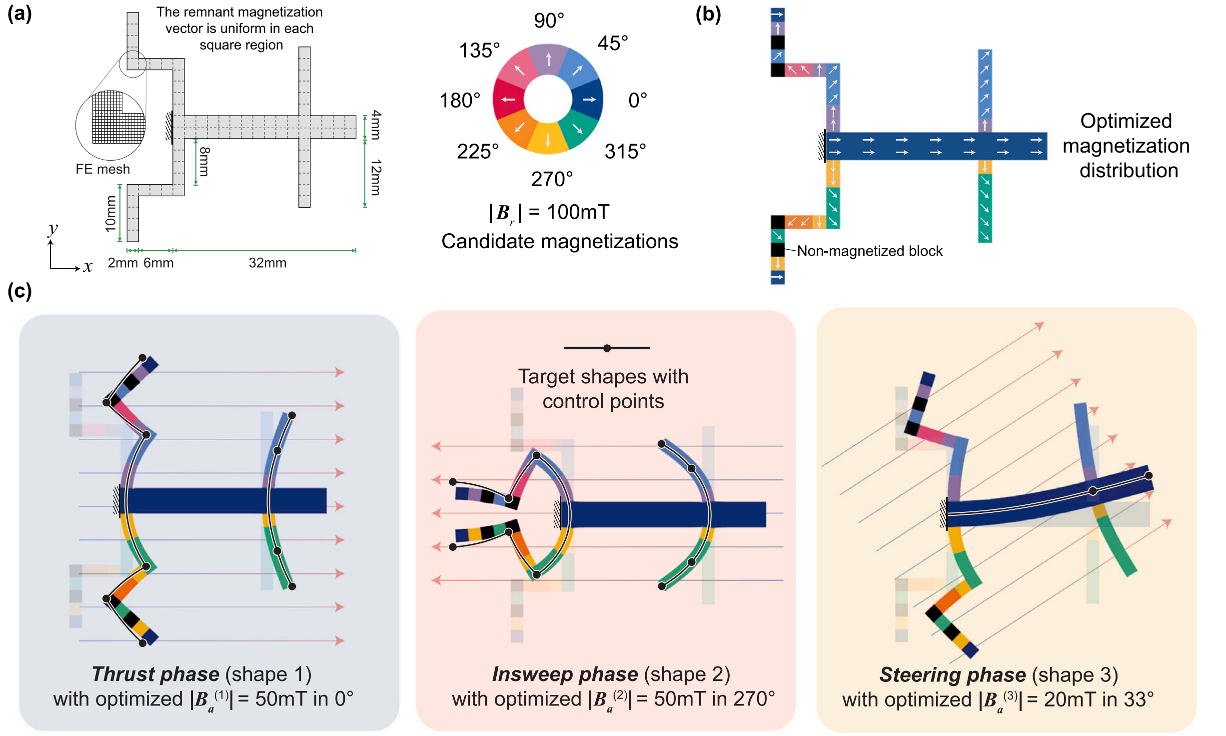

Fig. 4. Frog-inspired swimming robot: (a) Design domain and candidate magnetizations; (b) Optimized remnant magnetization distribution; (c) Target and optimized encoded shapes under magnetic actuation.

45° and same magnitude of 250mT. Unlike Examples 1 and 2, the applied magnetic flux design $\boldsymbol{B}_a$ is fixed to be pointing upward with a magnitude of 160mT throughout the optimization. For all the results represented in this example, we adopt initial guesses of $\xi_e^{(j)} = 1/8$, $j = 1, \ldots, 8$ and $\rho_e = v_{\max}$ (when we optimize topology) with $v_{\max} = 0.3$. The linear density filters ($q_\rho = q_m = 1$) are used with $R_\rho = R_m = 1.5$mm being the radius for both design variables ρ and $\xi^{(j)}$, $j = 1, \ldots, 8$.

4.2.1. Simultaneous optimization of matrix topology and remnant magnetization versus optimization of remnant magnetization distribution alone

The subsection of the example compares the actuation performance of the designs obtained by fixing topologies and only optimizing remnant magnetization distributions with that of the design obtained by optimizing both topology and remnant magnetization distribution simultaneously. Through comparison, we demonstrate that the incorporation of matrix topology variations enlarges the design space and leads to optimized designs with improved actuation performance.

An optimized actuator design is generated using the proposed formulation by simultaneously optimizing both matrix topology and remnant magnetization distributions. The maximum volume fraction of the actuator is set to be 30%. The optimized design and its deformed states under the applied magnetic field are shown in Fig. 5(b) (namely, Case 1). For comparison, we manually design four actuator topologies by experience and intuition (with the same 30% volume fraction), and then we optimize their remnant magnetization distributions. Fig. 5(c) (namely, Cases 2–5) depicts the optimized designs with their remnant magnetization distributions together with their deformed shapes under the applied magnetic field. For all the cases, we set $k_{\text{out}} = 0.2$N/mm and $|\boldsymbol{B}_a| = 160$mT.

The comparison of optimized designs in Fig. 5 shows that optimizing both matrix topology and remnant magnetization distribution simultaneously produces optimized designs with apparently improved actuation performance (measured by a larger $\bar{u}_{\text{out}}$) over the ones with intuitively-designed topologies (even with optimized remnant magnetization distributions). We further make several observations to elucidate how topology variation and large deformations are exploited by the optimization algorithm to enhance the actuation performance. First, the better actuation performances of Cases 4–5 than those of Cases 2–3 makes it evident that designs with more intricate topologies typically have larger actuation displacements. Second, we notice that both member rotation and bending deformations induced by the local magnetic torque can serve as actuation mechanisms. Varying the topology of the actuator can switch between these two mechanisms. For example, the actuation modes of designs in Cases 2–4 are dominated by bending deformations, whereas the designs in Cases 1 and 5 are mainly actuated by large rotations of certain members. The comparison of $\bar{u}_{\text{out}}$ for those designs suggests that the large rotation-based actuation mechanism is in general more effective than the

Table 2
Design parameters and the resulting actuated displacements of the optimized designs for Example 3 ($v_{\max}$ and $\sigma_{\max}$ are the upper bounds of volume fraction and von Mises stress, respectively; $|\boldsymbol{B}_a|$ is the magnitude of the external magnetic flux destiny; k_{out} is the spring stiffness; $\bar{u}_{\text{out}}$ is the averaged output displacements).

Case	$\lvert\boldsymbol{B}_a\rvert$ (mT)	$\sigma_{\max}$ (MPa)	$v_{\max}$	k_{out} (N/mm)	$\bar{u}_{\text{out}}$ (mm)
1	160	–	0.3	0.2	2.50
6	40	–	0.3	0.2	1.42
7	80	–	0.3	0.2	1.98
8	120	–	0.3	0.2	2.50
9	160	0.3	0.3	0.2	1.87
10	160	0.4	0.3	0.2	2.25
11	160	0.5	0.3	0.2	2.30
12	160	0.6	0.3	0.2	2.40
13	160	–	0.2	0.2	1.65
14	160	–	0.4	0.2	3.18
15	160	–	0.5	0.2	3.73
16	160	–	0.3	0.1	4.46
17	160	–	0.3	0.3	1.73
18	160	–	0.3	0.4	1.32

ones based on bending deformations. Third, a closer comparison of the optimized remnant magnetization distributions of the designs shows that the local magnetizations of those bending-actuated designs (i.e., Cases 2–4) are typically perpendicular to the applied $\boldsymbol{B}_a$ in their undeformed states, whereas the local magnetizations in some regions of the rotation-actuated designs (Cases 1 and 5) are different. Instead, those local magnetizations are rotated together with the underlying members under the applied magnetic field and become almost orthogonal to the $\boldsymbol{B}_a$ in the deformed configurations. This observation suggests that, when accounting for large deformations, setting the local magnetization vector to be orthogonal to the applied magnetic flux density $\boldsymbol{B}_a$ in the undeformed configuration is not necessarily optimal, because local magnetization will be closely interacting with the local structural deformation and be rotated accordingly in the deformed configuration. We remark that such behavior related to finite rotation cannot be captured by topology optimization formulations under small deformation assumptions. Finally, the design obtained by optimizing both matrix topology and remnant magnetization distribution simultaneously (i.e., Case 1) not only exhibits an actuation mechanism based on large rotations of members but also has bulkier rotated members (as compared to designs whose topologies are not optimized) to increase the actuation forces generated. As a result, this design achieves the largest actuated displacement among all designs.

4.2.2. Influences of design parameters on optimized results and corresponding mechanisms

In this subsection, we restrict our attention to the simultaneous optimization of matrix topology and remnant magnetization distribution and investigate the influences of various design parameters, including the magnitude of applied magnetic flux density $|\boldsymbol{B}_a|$, stress upper bound $\sigma_{\max}$, volume fraction $v_{\max}$, and spring stiffness k_{out}, on the optimized designs as well as their actuated displacement $\bar{u}_{\text{out}}$. In addition to the design Case 1 considered in the preceding subsection, we also use the optimization framework to generate design Cases 6–18 with different design parameter choices. Those choices are summarized in Table 2 for each design case. The parameters that are not listed in the table are taken to be the same as Case 1 described in the preceding subsection.

The influences of the four design parameters on $\bar{u}_{\text{out}}$ are shown in Fig. 6(a)–(d). Fig. 6(a) shows the influence of $|\boldsymbol{B}_a|$. We observe that $\bar{u}_{\text{out}}$ increases with $|\boldsymbol{B}_a|$ as a result of the larger magnetic torques generated. We also notice that, only two candidate magnetization vectors (pointing to 0° and 180°) are selected when $|\boldsymbol{B}_a|$ is small (i.e., 40mT). This is in contrast to the cases for larger $|\boldsymbol{B}_a|$ (i.e., 80mT–160mT), where four candidate magnetization vectors are selected (with two additional pointing to 225° and 315°). This contrast in optimized distribution reveals how the magnitude of applied magnetic field influences the optimized remnant magnetization distribution together with large deformations. Under the applied magnetic field with a small magnitude, the deformations level is relatively small and the remnant magnetization with orthogonal $\boldsymbol{B}_r$ and $\boldsymbol{B}_a$ is more effective for actuation. This phenomenon, however, does not hold for the applied magnetic field with a large magnitude, which requires the analysis of these quantities in the deformed configuration as a result of large deformations induced (in particular rotations). Fig. 6(b) shows the influence of the stress upper bound $\sigma_{\max}$. We observe that $\bar{u}_{\text{out}}$ of the optimized design increases if a larger $\sigma_{\max}$ is used. We also notice that the optimized remnant magnetization distributions are different for designs obtained with lower and higher stress upper bounds. Similar to the magnitude of $|\boldsymbol{B}_a|$, this is because a tighter allowable stress limit corresponds to a smaller allowable local deformation level, which prevents the members in the optimized design from experiencing large rotations. Fig. 6(c) shows the influence of allowable volume fraction $v_{\max}$. We observe a general trend that a larger $v_{\max}$ leads to an optimized design with higher $\bar{u}_{\text{out}}$. This trend can be understood by the body force nature of the magnetic torques generated in hard-magnetic soft materials. A design with a larger material volume experiences stronger magnetic torque in total and therefore has a larger actuated displacement. Unlike $|\boldsymbol{B}_a|$ and $\sigma_{\max}$, we notice that varying $v_{\max}$ greatly influences the optimized topology but does not impact the optimized remnant magnetization distributions (see designs in Cases 1, 13, 14, and 15). This is because varying the allowable volume fraction of the design does not affect the allowable deformation level. With the smallest allowable volume $v_{\max} = 20\%$, larger member rotations can still be achieved together with a topology containing hinge-like connections which concentrate local deformations. Fig. 6(d) shows the influence of spring stiffness k_{out}. We observe that $\bar{u}_{\text{out}}$ decreases as we increase the value of k_{out} as a result of increased feedback forces. Unlike other design parameters, we notices that varying the spring stiffness k_{out} does not lead to

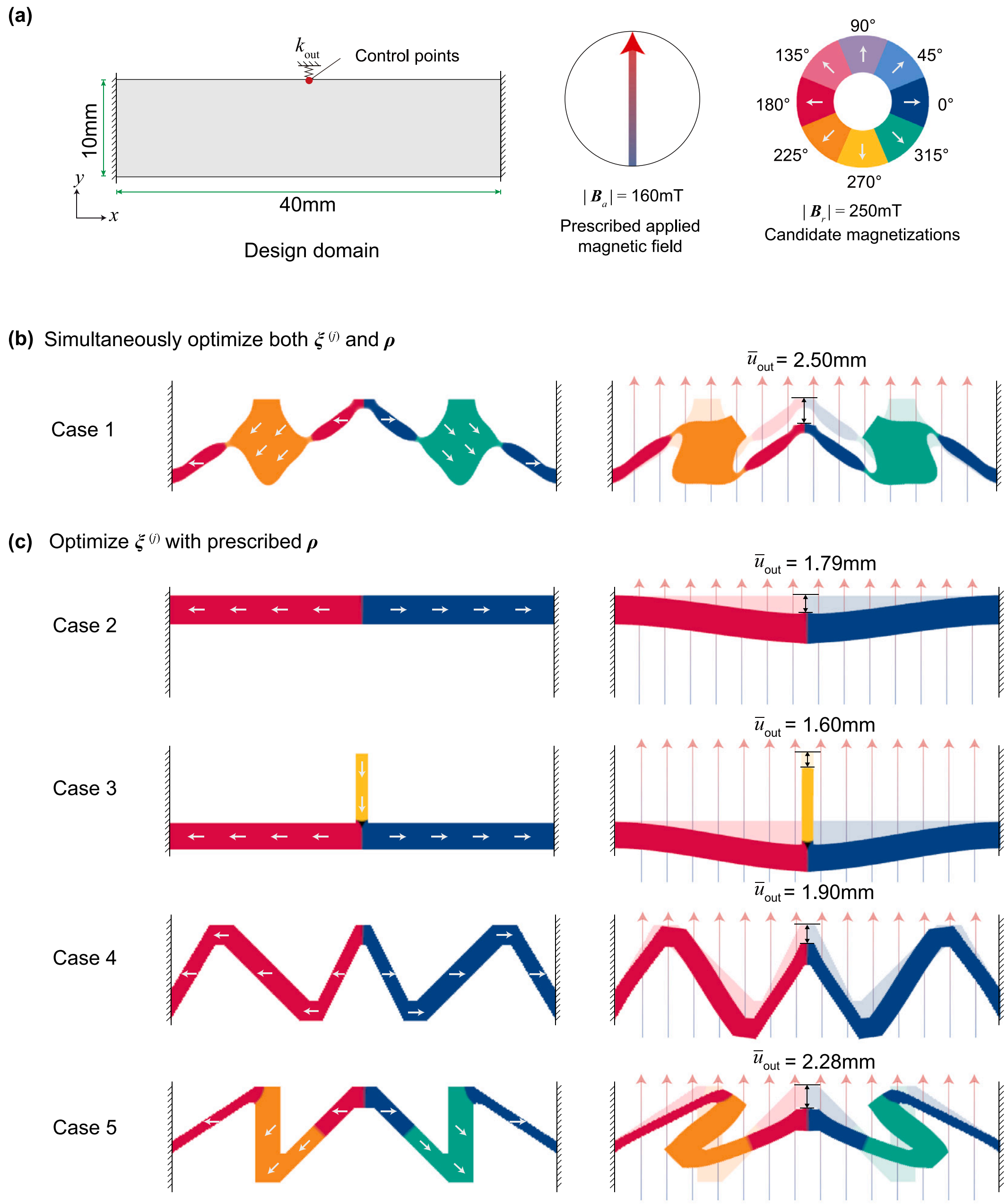

Fig. 5. Magnetic-responsive double-clamped actuator: (a) Design domain and candidate magnetizations; (b) Undeformed and deformed configurations of the designs with optimized ρ and $\xi^{(j)}$; (c) Undeformed and deformed configurations of the designs with prescribed ρ and optimized $\xi^{(j)}$.

significant changes in both the optimized topology and optimized remnant magnetization distribution (see designs in Cases 1, 16, 17, and 18).

To conclude, we emphasize that large deformations and, particularly, large rotation kinematics play an important role in how those design parameters (in particular $|\boldsymbol{B}_a|$ and $\sigma_{\max}$) impact the matrix topologies and remnant magnetization distributions of the optimized designs as well as their actuation performance. Our proposed topology optimization framework, formulated based on finite deformation kinematics, is able to capture those influences effectively.

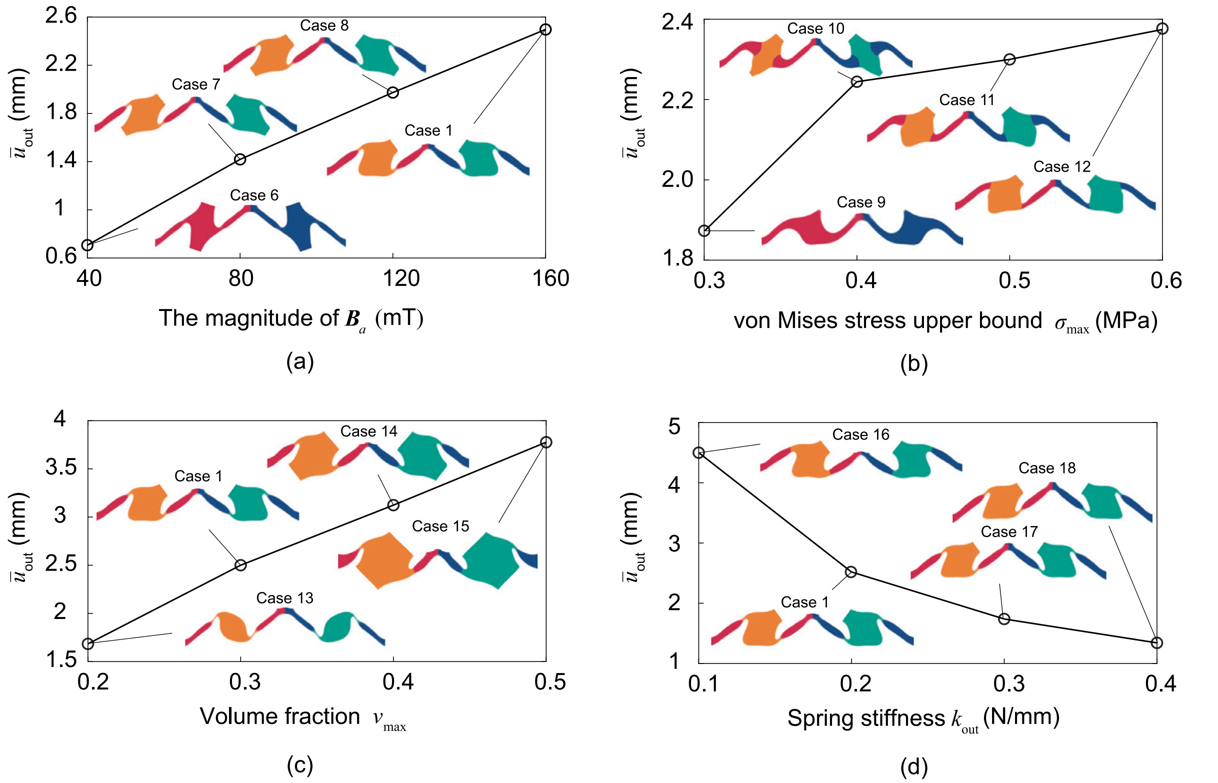

Fig. 6. Influences of physical design parameters on the optimized topologies and actuated displacements: (a) The magnitude of $\boldsymbol{B}_a$; (b) The upper bound of von Mises stress constraint $\sigma_{\max}$; (c) The upper bound of volume constraint, $v_{\max}$; (d) Spring stiffness, k_{out}.

4.3. Example 4: Magnetic actuators optimized with various local magnetization regions

This example designs and studies magnetic actuators which are only magnetized locally. We demonstrate that, by assigning different local magnetization zones, the proposed formulation can generate a variety of alternative actuator designs, which have different topologies and remnant magnetization distributions to achieve comparable performances with different actuation mechanisms. The design scenarios studied in the example could be useful in applications in which magnetizing the entire structure or applying the magnetic field to the entire design space is not permitted.

We consider a rectangular design domain with its dimensions and boundary conditions shown in Fig. 7. The design domain is discretized by $240 \times 160 = 38,400$ quadrilateral finite elements. Similar to the preceding example, we connect springs (in the x direction only) to finite element nodes surrounding the center on the right side of the domain. The total stiffness of those springs are summed to be $k_{\text{out}} = 0.02$N/mm. We treat the finite element nodes as the control points (i.e., $N_\alpha^{(1,2,\ldots,N_\ell)} = 5$) and minimize their displacements, averaged as $\bar{u}_{\text{out}}$, in the x direction (corresponding to maximizing the displacement in the opposite direction). The objective function $f_2(\cdot)$ in Eq. (16) is used together with $N_\ell = 1$, and the applied magnetic field is prescribed to be pointing in the negative x direction with a magnitude of 50mT. The matrix material is modeled by the compressible Ogden model with $\mu_a = 0.33$MPa, $\alpha_a = 2$, and $\beta_a = 499.5$, leading to $G = 0.33$MPa and $\kappa = 333$MPa. In addition, we consider two different local magnetization zone setups (with the same total area of 6mm^2) as shown in Fig. 7(b). The remnant magnetization at each location of the magnetization zones is selected by the optimizer from $N_m = 8$ candidate magnetization vectors, which are 45° apart from each other and have the same magnitude of 200mT. The materials outside of the magnetization zone are assumed to be non-magnetized and are not responsive to the applied magnetic field.

The results presented in this example are obtained by simultaneously optimizing matrix topology and remnant magnetization in the assigned magnetization zones with a stress upper bound of $\sigma_{\max} = 0.5$MPa. The initial guesses of design variables are $\xi_e^{(j)} = 1/8$, $j = 1, \ldots, 8$ and $\rho_e = v_{\max,1}$ with $v_{\max,1} = 25\%$. We apply a quadratic filter ($q_\rho = 2$ in Eq. (8)) to design variables $\boldsymbol{\rho}$ with a radius of $R_\rho = 1.2$mm and a linear filter ($q_m = 1$) to design variables $\boldsymbol{\xi}^{(j)}$, $j = 1, \ldots, 8$, with a radius of $R_m = 1$mm. We note that the quadratic filter is used for $\boldsymbol{\rho}$ to obtain well-defined boundaries of the resulting topology in this example. In addition, to prevent materials from concentrating in the magnetization zones by forming highly bulky members, we introduce a second volume constraint, namely, $(\sum_{i\in\mathcal{M}} v_i \bar{\rho}_i)/|\Omega_h| \leq v_{\max,2}$, with $\mathcal{M}$ being the element set of the magnetization zone and $v_{\max,2} = 15\%$.

The optimized designs obtained from Cases 1 and 2 and their corresponding $\bar{u}_{\text{out}}$ are presented in Fig. 8(a). We notice that the two designs achieve actuation via different topologies and remnant magnetization distributions. For the design in Case 1, magnetic

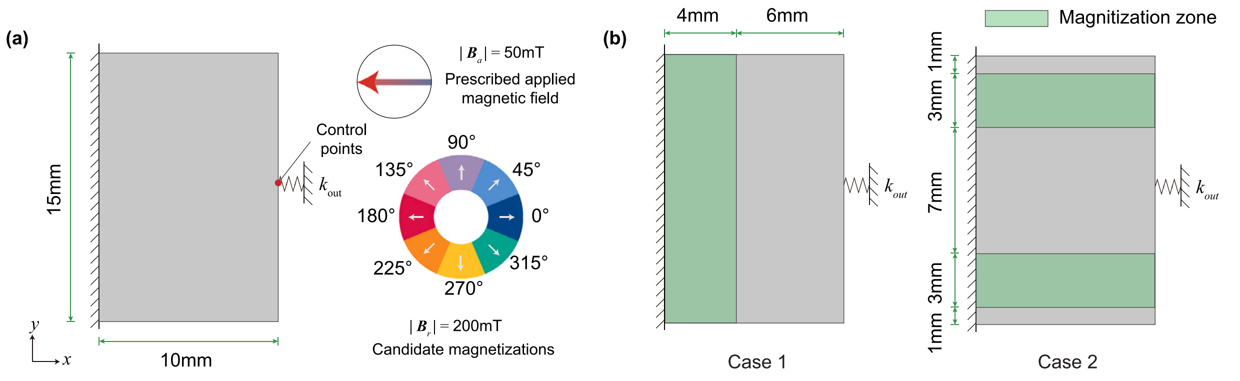

Fig. 7. Magnetic actuator: (a) Design domain, applied magnetic field, and candidate magnetizations; (b) Two cases with different magnetization zones.

torque-induced rotations are first generated in the four magnetized members on the left portion and then transmitted to the output location via three non-magnetized members. Instead, for the design obtained in Case 2, the magnetized members in both top and bottom regions experience gripping-type deformations, which are then transformed into a pulling motion in the non-magnetized member in the middle region to trigger displacement at the output location. Although having distinct topologies and remnant magnetization distributions, both optimized designs achieve comparable actuation performance, which demonstrates the capability of the proposed optimization framework in generating a variety of magnetic actuator designs with comparable performances by assigning various local magnetization zone layouts.

Moreover, Fig. 8(b) shows a representative convergence history of the objective function together with several intermediate designs to demonstrate how designs evolve in the proposed optimization formulation. First, we observe a smooth convergence of the objective function with each increase caused by the change of an optimization parameter in the continuation strategy.[1] Second, by monitoring how design evolves, we demonstrate that, at the beginning of optimization, the intermediate designs have blurred topologies and remnant magnetization distributions. As the SIMP penalization and Heaviside projection sharpness parameters increase, intermediate designs with crisper topologies and remnant magnetization distributions gradually appear until they reach an optimized design with binary topology and clearly-separated remnant magnetization distribution. Finally, we remark that the other examples presented in this paper show similar design evolution processes.

4.4. Example 5: Magnetic-responsive unit cell designs with programmable and adaptable actuation modes

This example uses the proposed topology optimization framework to discover magnetic-responsive unit cell designs that achieve various programmed actuation modes (including auxetic ones) that are adaptable under different applied magnetic fields. As shown in Fig. 9(a), we consider a square design domain which is fixed at its four corners. The design domain is discretized by $200 \times 200 = 40,000$ quadrilateral elements. The unit cell is surrounded by a 0.5mm-thick layer of non-magnetized materials which are treated as passive design regions throughout the optimization. We investigate three design scenarios, each is associated with multiple (i.e., $N_\ell > 1$) target actuation modes as illustrated in Fig. 9(b). In design scenario 1, the two adaptable target actuation modes correspond to expansion in either horizontal or vertical direction and contraction in the other, mimicking how materials with positive Poisson's ratios deform. In design scenario 2, the two target actuation modes correspond to either expansion or contraction in both directions, mimicking how materials with negative Poisson's ratios deform. In design scenario 3, we aim to discover a unit design that achieve all the above-mentioned four adaptable target modes (i.e., $N_\ell = 4$) under corresponding optimized applied magnetic fields. The optimization goal in the three scenarios is to maximize the deformation of the unit cell in those target actuation modes. To achieve that, we place one control point to the center of each side of the unit cell, namely $N_\alpha^{(\ell)} = 4$, $\ell = 1, 2, \ldots, N_\ell$. We monitor the vertical displacements associated with control points C_1 and C_2, and the horizontal displacements for control points C_3 and C_4. Those monitored displacements (incorporated with appropriate signs) are then used by the objective function $f_2(\cdot)$ (see Eq. (16)) to maximize certain actuation modes. The averaged absolute displacements of the four control points in the ℓ deformation mode, denoted as $|\bar{u}|_{\text{out}}^{(\ell)}$ hereafter, will be used to measure the performance of the optimized unit cells. A larger value of $|\bar{u}|_{\text{out}}^{(\ell)}$ indicates optimized unit cells with better magnetic-actuated performance.

We simultaneously optimize all three design variables, i.e., topology (matrix material distribution), remnant magnetization distribution, and the applied magnetic fields. The matrix material is modeled by the compression Ogden model with $\mu_a = 0.33$MPa, $\alpha_a = 2$, and $\beta_a = 499.5$, leading to $G = 0.33$MPa and $\kappa = 333$MPa. We consider a total of $N_m = 8$ candidate magnetization vectors

[1] The continuation strategies for p_ρ, p_m, β_ρ, and β_m are as follows: We first run for 100 iterations with $p_\rho = p_m = 1$ and $\beta_\rho = \beta_m = 1$. We then increase p_ρ and p_m together by 1 every 50 iterations until $p_\rho = 3$ and $p_m = 5$. Afterwards, we first double β_m every 50 iterations until $\beta_m = 32$ and then double β_ρ every 50 iterations until $\beta_\rho = 32$. We finally run 300 addition iterations before optimization reaches convergence.

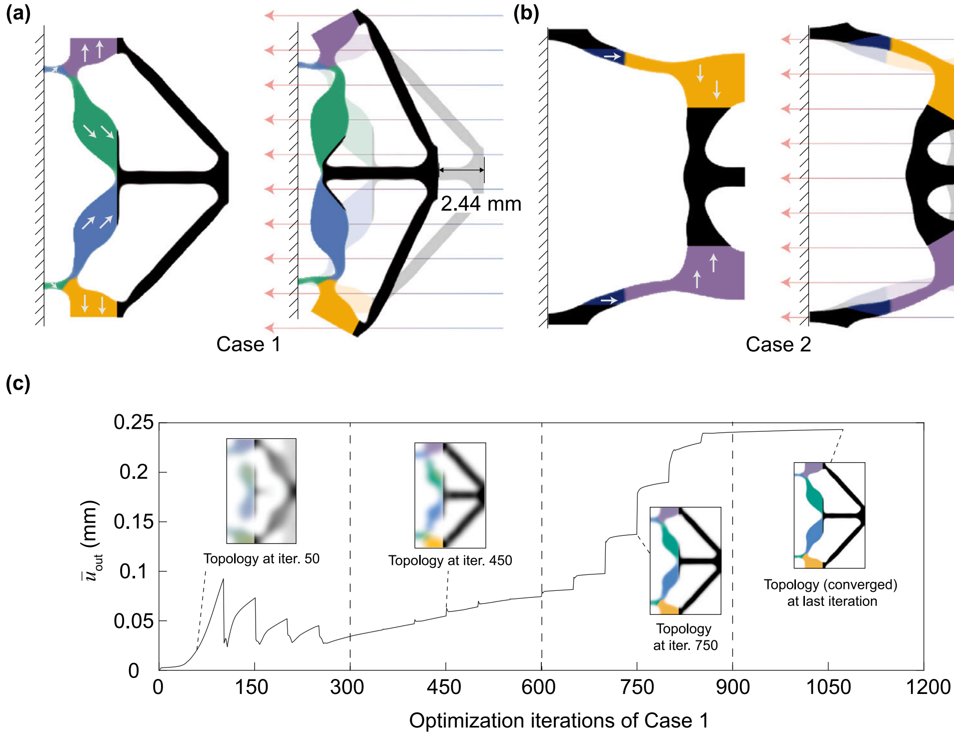

Fig. 8. Undeformed and deformed configurations of two designs (Cases 1–2) for magnetic actuators with different magnetization zones; (b) Optimization history and structural topology evolution of Case 1.

which are 45° apart from each other and have the same magnitude of 100mT. Multiple applied magnetic fields are needed — one for each target deformation mode. Since the goal is to maximize deformation, the magnitude of both applied magnetic flux densities $\boldsymbol{B}_a^{(\ell)}$ are set to be 50mT. In design scenarios 1 and 2, we fix the direction of $\boldsymbol{B}_a^{(1)}$ to be pointing downward and optimize the direction of $\boldsymbol{B}_a^{(2)}$ (the initial guess of $\boldsymbol{B}_a^{(2)}$ is assumed to point upward). In design scenario 3, we fix the directions of $\boldsymbol{B}_a^{(3,4)}$ to be pointing downward and upward, respectively, and optimize the directions of $\boldsymbol{B}_a^{(1,2)}$ (the initial guesses of $\boldsymbol{B}_a^{(1,2)}$ are assumed to point leftward and rightward, respectively). For optimization, we apply a quadratic filter ($q_\rho = 2$ in Eq. (8)) to design variables $\boldsymbol{\rho}$ with a radius of 0.75mm and a linear filter ($q_m = 1$) to design variables $\boldsymbol{\xi}^{(j)}$ with a radius of 1mm. We note that the quadratic filter is used for $\boldsymbol{\rho}$ to obtain well-defined boundaries of the resulting topology in this example. For all the designs, the allowable volume fraction is set to be $v_{\max} = 30\%$ (excluding the passive non-magnetized boundary layer). Based on our numerical experience, the stress upper bounds are taken to be $\sigma_{\max}^{(1)} = \sigma_{\max}^{(2)} = 0.25$MPa for design scenarios 1 and 2 as well as $\sigma_{\max}^{(1)} = \sigma_{\max}^{(2)} = \sigma_{\max}^{(3)} = \sigma_{\max}^{(4)} = 0.2$MPa for design scenario 3. In addition, the initial guesses of the design variables $\xi_e^{(j)}, j = 1, \ldots, 8$, are set to be uniformly 1/8 in the domain.

Figs. 10(a)–(b) show optimized designs, in both undeformed and deformed configurations, obtained for design scenarios 1 and 2, respectively. For each scenario, we consider two types of initial guesses for the topology design variables $\boldsymbol{\rho}$, which are depicted in the first column of Fig. 10. For Scenario 1, the optimized design obtained from the uniform initial guess of $\boldsymbol{\rho}$ contains four magnetized members, each attached to two neighboring sides of the non-magnetized boundary layer. These magnetized members rotate under the applied magnetic fields, causing the non-magnetized boundary layer to bend accordingly to generate displacements in the control points. By contrast, the four magnetized members in the optimized design obtained from the non-uniform initial guess of $\boldsymbol{\rho}$ (i.e., four squares) are isolated in the center of the unit cell and their induced rotations are transferred to each control point via small axial members under tension or comparison. For Scenario 2, the optimized design obtained from the uniform initial guess of $\boldsymbol{\rho}$ contains eight magnetized members, each attached to only one side (as compared to two sides in the counterpart in Scenario 1) of the non-magnetized layer. These members experience rotations under the applied magnetized fields, which bend the non-magnetized layer to actuate the corresponding actuation modes. In fact, designs with similar actuation mechanisms are also presented in the literature (Montgomery et al., 2021; Wu et al., 2019). Instead, the optimized design obtained from the non-uniform initial guess of $\boldsymbol{\rho}$ (i.e., one square) possesses more intricate topologies and remnant magnetization distributions. Four larger magnetized members appear in the center region of the domain and experience large rotations under the applied magnetic fields. These large rotations are then transferred to the control points in the x direction by four smaller magnetized members rotating in the opposite directions and the ones in the y direction by two axial members under tension or compression. This asymmetry of topology, magnetized distribution, and actuation mechanisms in the x and y directions is a consequence of the asymmetry of the applied magnetic flux densities $\boldsymbol{B}_a^{(1)}$ and $\boldsymbol{B}_a^{(2)}$, which are both in the vertical direction.

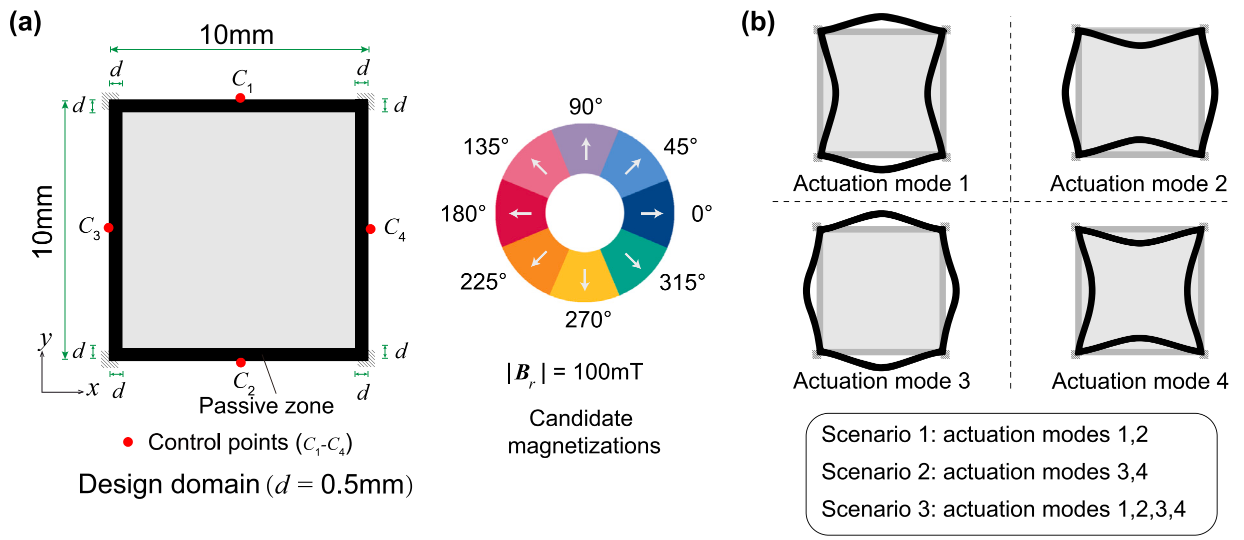

Fig. 9. Unit cell design: (a) Design domain and candidate magnetizations; (b) Three design scenarios (each has multiple deformed modes to be achieved under different magnetic fields).

In Fig. 11, we show the optimized design and the four adaptable modes under corresponding optimized magnetic fields for Scenario 3. Similar to the actuation mechanism of the last design in Fig. 10, four central magnetized members rotate under applied magnetic fields, and the rotations are transferred to non-magnetized layers through four magnetized members in the x direction and two small non-magnetized members in the y direction. Different from the designs in Fig. 10, the local remnant magnetization distribution is neither fully orthogonal nor parallel to the applied magnetic fields, which is relatively non-intuitive and demonstrates that encoding an increased number of target deformation modes in Scenario 3 makes the optimization problem more complex.

Comparing the designs in Fig. 10, we conclude that different initial designs lead to magnetic-responsive optimized unit cells with different topologies, remnant magnetization distributions, and actuation mechanisms, which is a demonstration of the non-convexity of the optimization formulation. Although it may not be generalizable to other design scenarios, we find that a non-uniform initial guess for $\boldsymbol{\rho}$ always leads to optimized designs with better actuation performances as compared to uniform initial guesses in this example. We also find that, in design scenarios 1 and 2, the optimized applied magnetic flux density $\boldsymbol{B}_a^{(2)}$ always point to the opposite direction of $\boldsymbol{B}_a^{(1)}$, which is fixed throughout the optimization. For design scenario 3, the directions of optimized applied magnetic flux densities $\boldsymbol{B}_a^{(1)}$ and $\boldsymbol{B}_a^{(2)}$ are close to being opposite (19° and 196°) to each other. These findings suggest that by reversing the applied magnetic field, one can obtain an opposite deformation mode (i.e., control points all point to opposite directions) in this example. Moreover, we remark that this example demonstrates that the proposed topology optimization framework can lead to a promising path toward the automatic discovery of magnetic-responsive metamaterials with various unconventional yet programmable actuation modes and nonlinear behaviors under the optimized applied magnetic fields.

5. Conclusion

This work proposes a general topology optimization framework for the rational design of hard-magnetic soft materials and structures by simultaneously optimizing their matrix topologies, remnant magnetization distributions, and applied magnetic fields. The framework is built upon the nonlinear field theory for ideal hard-magnetic soft materials (Zhao et al., 2019). We first propose a design parameterization scheme that represents matrix material topology, remnant magnetization distribution, and the applied magnetic field using three sets of design variables. In particular, the remnant magnetization vector at each location of the design is interpolated from a set of pre-defined candidate vector (with the same magnitude) and is promoted to converge towards one (and only one) of the candidate vector at the end of the optimization. We then introduce a scheme to interpolate the Helmholtz free energy function from the three sets of design variables. The interpolated Helmholtz free energy function characterizes the nonlinear response of a given design under the applied magnetic field. We formulate the general optimization problem and consider two representative design objective functions, which aim to program deformed shapes and maximize magnetic actuations, respectively.

We present five examples with various optimized magnetic-responsive designs to exemplify the potential applications and demonstrate the capabilities of the proposed topology optimization framework. In the first and second examples, we simultaneously optimize the remnant magnetization distribution and applied magnetic fields to generate a magnetic-responsive arm and a frog-inspired swimming robot that achieve multiple target deformed shapes under optimized magnetic fields. The demonstrated

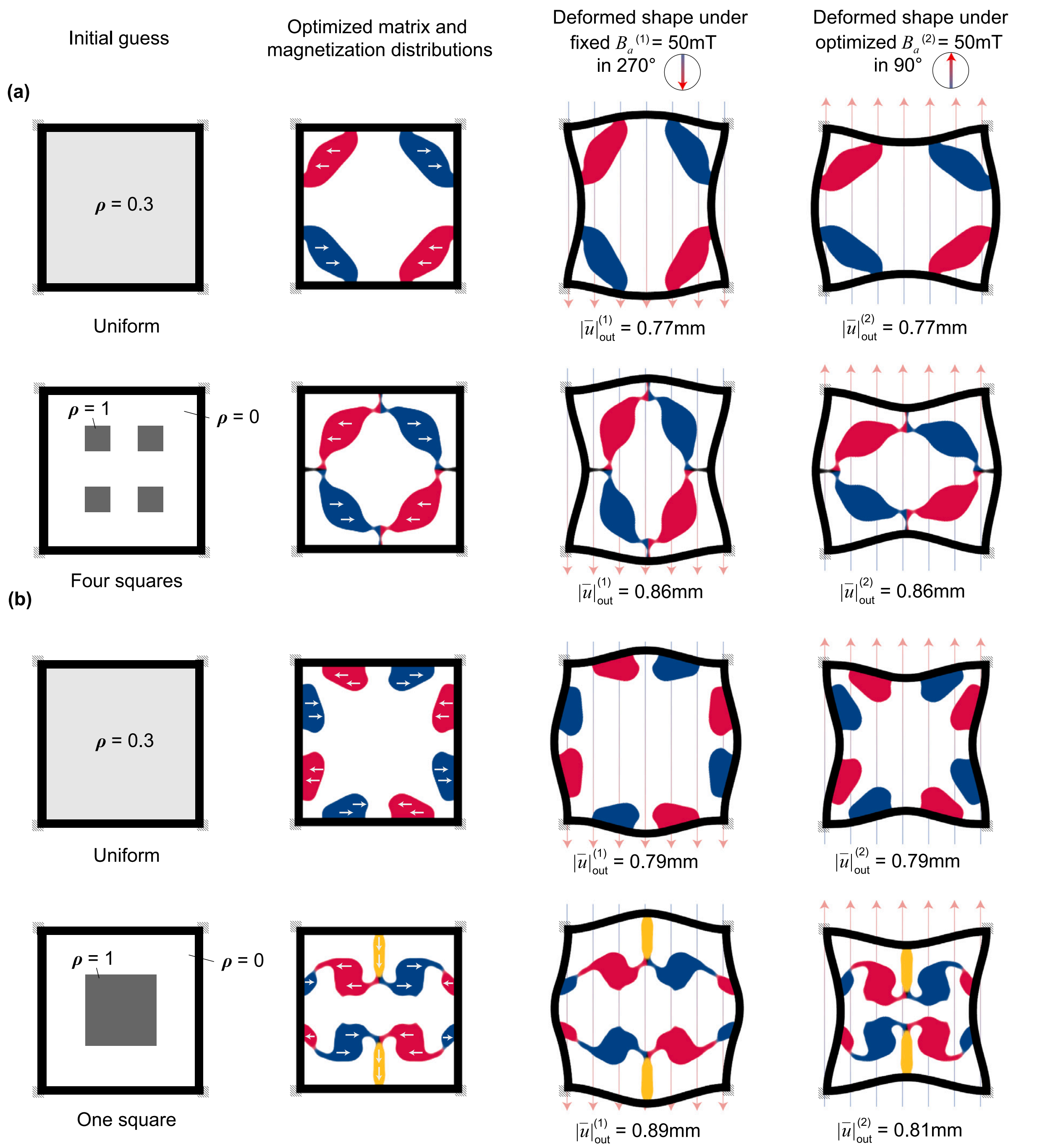

Fig. 10. The initial guesses, optimized designs, and corresponding adaptable actuation modes of magnetic-responsive unit cells for (a) Scenario 1 and (b) Scenario 2, mimicking how materials with positive and negative Poisson's ratios deform, respectively. See Fig. 9 for actuation modes associated with each scenario.

capability of the proposed framework in generating highly programmable magnetic-responsive metastructures holds great potential in various applications related to soft robotics.

In the third example, we design double-clamped actuators with maximized magnetic actuation performance to highlight the importance of optimizing the matrix topology. We also demonstrate that large deformations and, particularly, large rotations, which are accounted for in the proposed framework, play important roles in determining both the optimized topologies and optimized

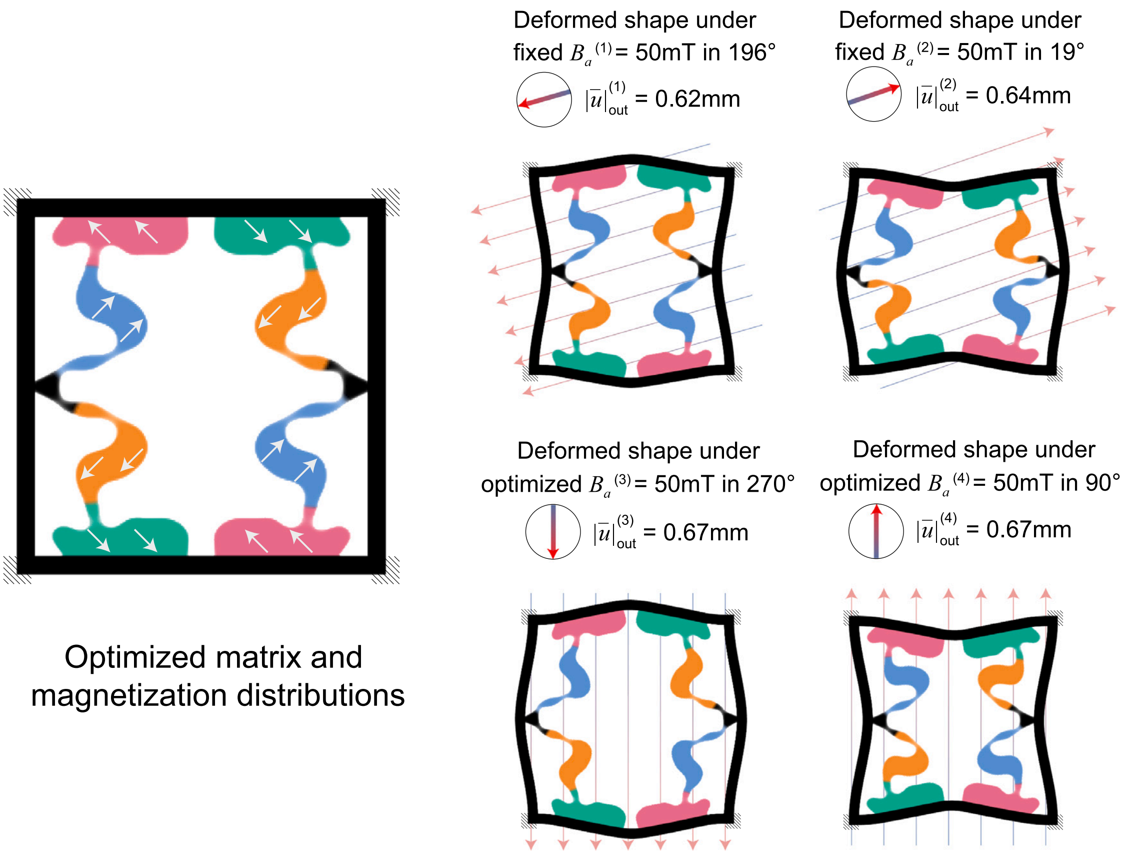

Fig. 11. The optimized magnetic-responsive unit cell design and four adaptable actuation modes (Scenario 3). See Fig. 9 for actuation modes associated with each scenario.

remnant magnetization distributions. In the fourth example, we present designs of magnetic actuators which are magnetized locally. By varying the prescribed magnetization zones, designs with various topologies and remnant magnetization distributions are generated, which can achieve comparable actuation performance. Together, Example 3 and 4 showcase the proposed framework offers an effective design tool to discover efficient magnetic actuators for various applications.

In the last example, we apply the proposed framework to explore magnetic-responsive unit cell designs capable of achieving various programmable and several adaptable actuation modes under different magnetic fields (mimicking how materials with positive and negative Poisson's ratios deform) by simultaneously optimize all design variables. Multiple designs with unconventional optimized topologies and remnant magnetization distributions are generated by varying optimization initial guesses, demonstrating the effectiveness of the proposed methodology to explore various designs with distinct mechanisms. This example also demonstrates that the proposed framework holds the potential to enable a path towards the automatic discovery and rational design of metamaterials with unconventional yet highly programmable magneto-mechanical behaviors.

Finally, we make several remarks on the future directions of the present work in terms of design parameterization, modeling, and validation aspects. In terms of design parameterization and modeling, for hard-magnetic soft materials structures with non-uniform remnant magnetization distributions, the presence of the surrounding air has non-negligible influence on the local distributions of magnetic fields (i.e., $\boldsymbol{B}$ and $\boldsymbol{H}$) in the structure (Mukherjee et al., 2021). Thus, an important future extension of the present work is to include the surrounding air in both design parameterization and modeling (Psarra et al., 2019) parts of the framework. In terms of manufacturing and experimental validation, we remark that the proposed formulation in this study does not explicitly incorporate manufacturing considerations, such as the minimum feature sizes of each structural member and magnetization region, the manufacturable complexity of magnetization distributions and structural topologies, and the influence of manufacturing errors on the performance of the optimized designs. Therefore, the realization of the optimized designs via advanced manufacturing techniques (and further experimental validation of their performance) are important directions of future work.

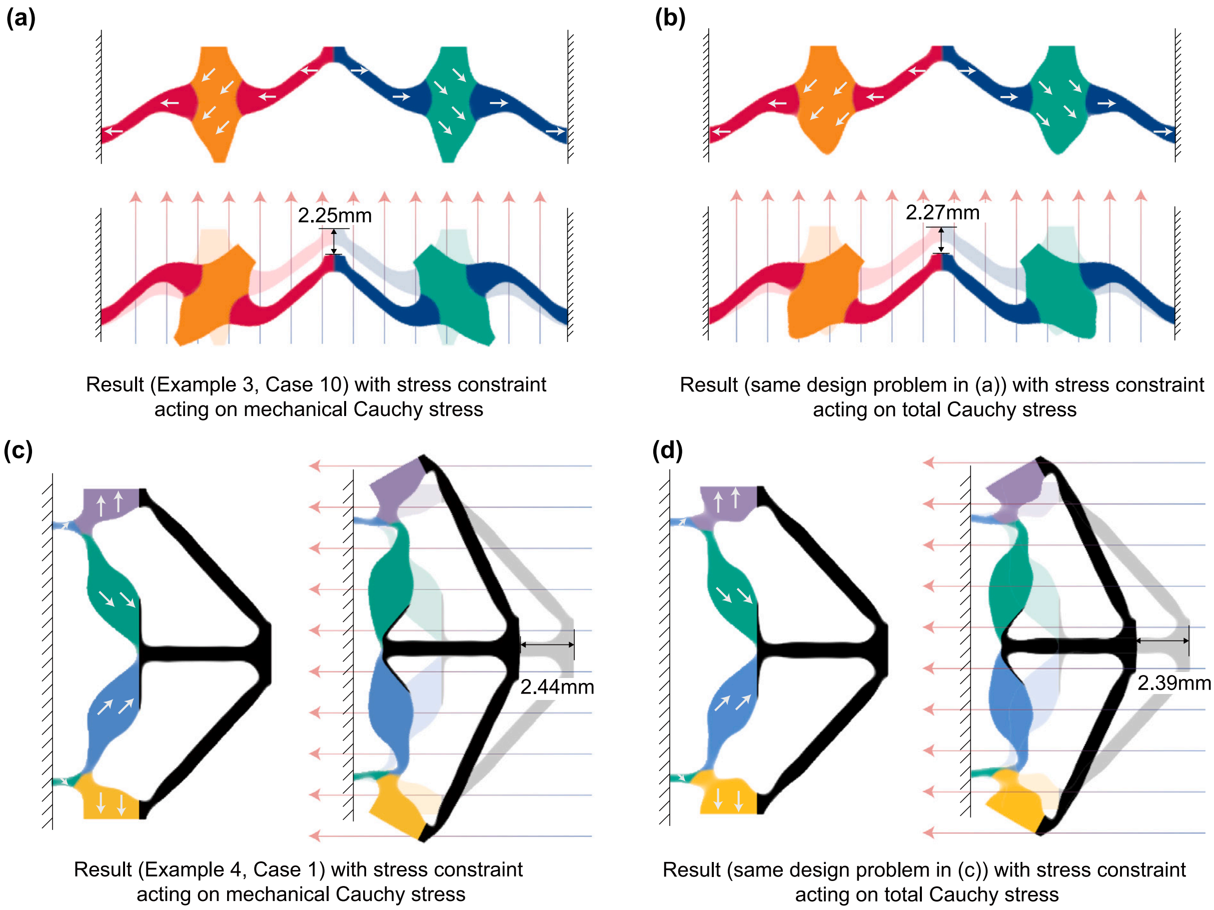

Fig. 12. Comparisons of two stress constraints: The designs of magnetic actuator obtained by the stress constraint acting on (a) mechanical Cauchy stress and (b) total Cauchy stress. The designs of magnetic actuators (with non-magnetized zones) obtained by the stress constraint acting on (c) mechanical Cauchy stress and (d) total Cauchy stress.

CRediT authorship contribution statement

Zhi Zhao: Investigation, Software, Writing – original draft, Writing – review & editing. **Xiaojia Shelly Zhang:** Conceptualization, Supervision, Investigation, Writing – original draft, Writing – review & editing, Funding acquisition.

Declaration of competing interest

The authors declare that they have no known competing financial interests or personal relationships that could have appeared to influence the work reported in this paper.

Acknowledgment

The authors acknowledge the financial support from the U.S. National Science Foundation (NSF) CAREER Award CMMI-2047692. The information provided in this paper is the sole opinion of the authors and does not necessarily reflect the view of the sponsoring agency.

Appendix A. Alternative stress constraint

This appendix presents an alternative stress constraint serving as a numerical technique to prevent hinge-like connections (or thin members) from appearing in the optimized designs. Rather than using the stress constraint reported in Eq. (14) which restricts the

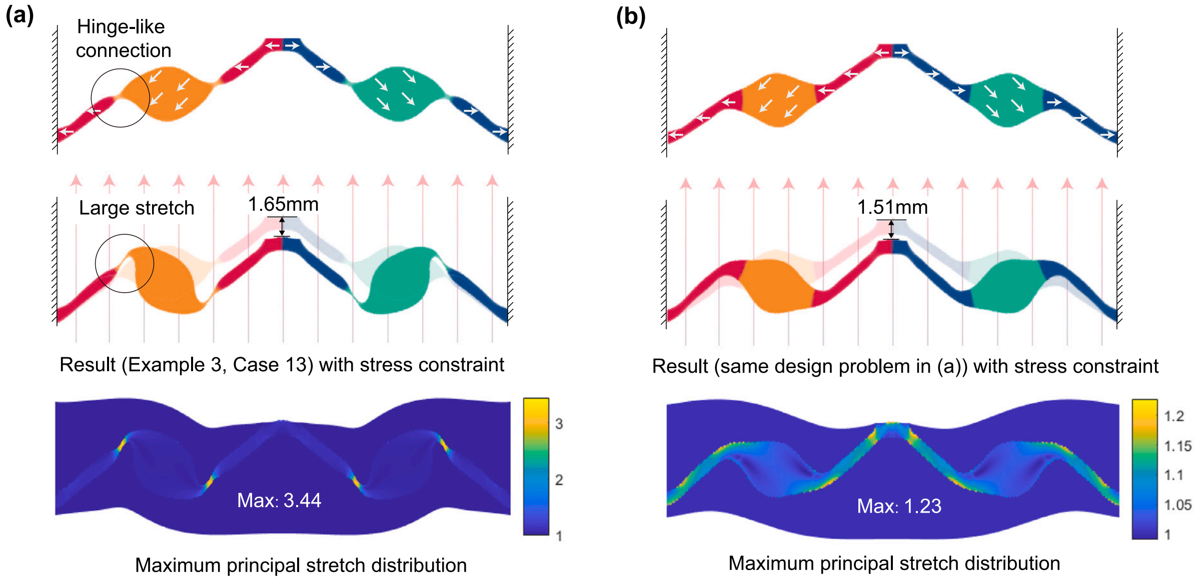

Fig. 13. Comparison of topologies, deformations, and maximum principal stretch distributions for the designs obtained (a) without the stress constraint and (b) with the stress constraint (stress upper bound is 0.4MPa).

mechanical Cauchy stress ($\boldsymbol{\sigma}_E$), the alternative constraint acts on the total Cauchy stress (involving both mechanical and magnetic Cauchy stresses), which is given by

$$\left\{ \sum_{e=1}^{N_e} \left[\frac{w_\sigma(\overline{\rho}_e)}{v_e} \int_{\Omega_{h,e}} \sigma_{\mathrm{VM}}\left(\boldsymbol{\sigma}_T\left(\boldsymbol{u}^{(\ell)}, \xi, \boldsymbol{B}_a^{(\ell)}\right)\right) \mathrm{d}\boldsymbol{X} \right]^{p_n} \right\}^{1/p_n} \le \sigma_{\max}^{(\ell)}, \quad \ell = 1, \ldots, N_\ell, \tag{21}$$

where $\boldsymbol{\sigma}_T = 1/J(\partial W(\boldsymbol{F})/\partial \boldsymbol{F})\boldsymbol{F}^T$ is total Cauchy stress, which is a asymmetric tensor (Zhao et al., 2019). Other variables in Eq. (21) are the same as the ones described in Eq. (14).

We perform a comparison of the optimized designs obtained from the two stress constraints in Fig. 12. The designs in Fig. 12(a) and (c) are the same as the ones in Case 10 of Example 3 and Case 1 of Example 4, respectively, which are obtained using the stress constraint acting on the mechanical Cauchy stress. As shown in Fig. 12(b) and (d), we use the same design setups and employ the stress constraint imposing on the total Cauchy stress to obtain magnetic actuator designs, with the stress upper bounds 0.45MPa and 0.40MPa, respectively. From the two pairs of designs, i.e. (a) versus (b), and (c) versus (d), we find that the matrix and magnetization distributions as well as the actuated displacements are similar, and no hinge-like connections are generated in all the designs. Therefore, we conclude that both stress constraints are capable of generating hinge-free designs and avoiding excessive local deformations (their effectiveness is further demonstrated in Appendix B). We highlight that the two stress constraints purely serve as a numerical technique to prevent hinge-like connections of the optimized designs in this study, and whether the two stress constraints capture physical material failure remains future investigations.

Appendix B. Effectiveness of the stress constraint to prevent hinge-like connections

This appendix demonstrates that the applied stress constraint effectively eliminates hinge-like connections (or thin members), which can lead to excessively large deformations. We compare two designs of the double-clamped actuator (Example 3, Case 13) generated without and with the stress constraint (stress upper bound is 0.40MPa), respectively. As shown in Fig. 13(a), the design without stress constraint generates hinge-like connections between the central bulky members and their surrounding bars. Under the applied magnetic field, these hinge-like connections are stretched excessively with a maximum principal stretch of 3.44. On the contrary, the design with stress constraint in Fig. 13(b) has no hinge-like connections with a lower maximum principal stretch of 1.23. Even though the hinge-free design obtained with the stress constraint induces a smaller actuated displacement than the design obtained without the stress constraint, it can avoid excessive local deformations and ease the manufacturing process. Through this comparison, we conclude that the applied stress constraint can effectively prevent hinge-like connections (or thin members) from being generated in the optimized designs with hard-magnetic soft materials.

References

Alapan, Yunus, Karacakol, Alp C, Guzelhan, Seyda N, Isik, Irem, Sitti, Metin, 2020. Reprogrammable shape morphing of magnetic soft machines. Sci. Adv. 6 (38), eabc6414.

Armijo, Larry, 1966. Minimization of functions having Lipschitz continuous first partial derivatives. Pacific J. Math. 16 (1), 1–3.

Bastola, Anil Kumar, Paudel, Milan, Li, Lin, Li, Weihua, 2020. Recent progress of magnetorheological elastomers: a review. Smart Mater. Struct..

Bendsøe, Martin P., 1989. Optimal shape design as a material distribution problem. Struct. Optim. 1 (4), 193–202.

Bendsoe, Martin Philip, Sigmund, Ole, 2013. Topology Optimization: Theory, Methods, and Applications. Springer Science & Business Media.

Bourdin, Blaise, 2001. Filters in topology optimization. Internat. J. Numer. Methods Engrg. 50 (9), 2143–2158.

Bruggi, Matteo, 2008. On an alternative approach to stress constraints relaxation in topology optimization. Struct. Multidiscip. Optim. 36 (2), 125–141.

Bruns, Tyler E., Tortorelli, Daniel A., 2001. Topology optimization of non-linear elastic structures and compliant mechanisms. Comput. Methods Appl. Mech. Engrg. 190 (26–27), 3443–3459.

Bruyneel, Michael, Duysinx, Pierre, 2005. Note on topology optimization of continuum structures including self-weight. Struct. Multidiscip. Optim. 29 (4), 245–256.

Chen, Tian, Pauly, Mark, Reis, Pedro M., 2021. A reprogrammable mechanical metamaterial with stable memory. Nature 589 (7842), 386–390.

Cheng, Gengdong, Jiang, Zheng, 1992. Study on topology optimization with stress constraints. Eng. Optim. 20 (2), 129–148.

Dorfmann, A., Ogden, R.W., 2003. Magnetoelastic modelling of elastomers. Eur. J. Mech. A Solids 22 (4), 497–507.

Duysinx, Pierre, Bendsøe, Martin P., 1998. Topology optimization of continuum structures with local stress constraints. Internat. J. Numer. Methods Engrg. 43 (8), 1453–1478.

Feng, Z.-Q., Peyraut, François, He, Q.-C., 2006. Finite deformations of ogden's materials under impact loading. Int. J. Non-Linear Mech. 41 (4), 575–585.

Hines, Lindsey, Petersen, Kirstin, Lum, Guo Zhan, Sitti, Metin, 2017. Soft actuators for small-scale robotics. Adv. Mater. 29 (13), 1603483.

Homayouni-Amlashi, Abbas, Schlinquer, Thomas, Mohand-Ousaid, Abdenbi, Rakotondrabe, Micky, 2020. 2D topology optimization MATLAB codes for piezoelectric actuators and energy harvesters. Struct. Multidiscip. Optim. 1–32.

Kim, Yoonho, Yuk, Hyunwoo, Zhao, Ruike, Chester, Shawn A, Zhao, Xuanhe, 2018. Printing ferromagnetic domains for untethered fast-transforming soft materials. Nature 558 (7709), 274–279.

Li, Weichen, Wang, Fengwen, Sigmund, Ole, Zhang, Xiaojia Shelly, 2021. Design of composite structures with programmable elastic responses under finite deformations. J. Mech. Phys. Solids 104356.

Lloyd, Peter, Hoshiar, Ali Kafash, da Veiga, Tomas, Attanasio, Aleks, Marahrens, Nils, Chandler, James Henry, Valdastri, Pietro, 2020. A learnt approach for the design of magnetically actuated shape forming soft tentacle robots. IEEE Robot. Autom. Lett. 5 (3), 3937–3944.

Lum, Guo Zhan, Ye, Zhou, Dong, Xiaoguang, Marvi, Hamid, Erin, Onder, Hu, Wenqi, Sitti, Metin, 2016. Shape-programmable magnetic soft matter. Proc. Natl. Acad. Sci. 113 (41), E6007–E6015.

Luo, Zhen, Tong, Liyong, Ma, Haitao, 2009. Shape and topology optimization for electrothermomechanical microactuators using level set methods. J. Comput. Phys. 228 (9), 3173–3181.

Montgomery, S Macrae, Wu, Shuai, Kuang, Xiao, Armstrong, Connor D, Zemelka, Cole, Ze, Qiji, Zhang, Rundong, Zhao, Ruike, Qi, H Jerry, 2021. Magneto-mechanical metamaterials with widely tunable mechanical properties and acoustic bandgaps. Adv. Funct. Mater. 31 (3), 2005319.

Mukherjee, Dipayan, Rambausek, Matthias, Danas, Kostas, 2021. An explicit dissipative model for isotropic hard magnetorheological elastomers. J. Mech. Phys. Solids 151, 104361.

Ogden, Raymond W., 1997. Non-Linear Elastic Deformations. Courier Corporation.

Olhoff, Niels, 1989. Multicriterion structural optimization via bound formulation and mathematical programming. Struct. Optim. 1 (1), 11–17.

Poulain, X, Lefevre, Victor, Lopez-Pamies, O, Ravi-Chandar, K, 2017. Damage in elastomers: nucleation and growth of cavities, micro-cracks, and macro-cracks. Int. J. Fract. 205 (1), 1–21.

Psarra, E., Bodelot, L., Danas, K., 2019. Wrinkling to crinkling transitions and curvature localization in a magnetoelastic film bonded to a non-magnetic substrate. J. Mech. Phys. Solids 133, 103734.

Qi, Song, Guo, Hengyu, Fu, Jie, Xie, Yuanpeng, Zhu, Mi, Yu, Miao, 2020. 3D printed shape-programmable magneto-active soft matter for biomimetic applications. Compos. Sci. Technol. 188, 107973.

Rozvany, George I.N., Zhou, Ming, Birker, Torben, 1992. Generalized shape optimization without homogenization. Struct. Optim. 4 (3–4), 250–252.

Ruiz, D., Sigmund, Ole, 2018. Optimal design of robust piezoelectric microgrippers undergoing large displacements. Struct. Multidiscip. Optim. 57 (1), 71–82.

Sigmund, Ole, 2001. Design of multiphysics actuators using topology optimization–part II: Two-material structures. Comput. Methods Appl. Mech. Engrg. 190 (49–50), 6605–6627.

Sigmund, Ole, 2007. Morphology-based black and white filters for topology optimization. Struct. Multidiscip. Optim. 33 (4–5), 401–424.

Sitti, Metin, 2018. Miniature soft robots—road to the clinic. Nat. Rev. Mater. 3 (6), 74–75.

Sundaram, Subramanian, Skouras, Melina, Kim, David S, van den Heuvel, Louise, Matusik, Wojciech, 2019. Topology optimization and 3D printing of multimaterial magnetic actuators and displays. Sci. Adv. 5 (7), eaaw1160.

Svanberg, Krister, 1987. The method of moving asymptotes—a new method for structural optimization. Internat. J. Numer. Methods Engrg. 24 (2), 359–373.

Tian, Jiawei, Zhao, Xuanhe, Gu, Xianfeng David, Chen, Shikui, 2020. Designing ferromagnetic soft robots (FerroSoRo) with level-set-based multiphysics topology optimization. In: 2020 IEEE International Conference on Robotics and Automation (ICRA). IEEE, pp. 10067–10074.

Venkiteswaran, Venkatasubramanian Kalpathy, Samaniego, Luis Fernando Pena, Sikorski, Jakub, Misra, Sarthak, 2019. Bio-inspired terrestrial motion of magnetic soft millirobots. IEEE Robot. Autom. Lett. 4 (2), 1753–1759.

Wang, Fengwen, Lazarov, Boyan Stefanov, Sigmund, Ole, 2011. On projection methods, convergence and robust formulations in topology optimization. Struct. Multidiscip. Optim. 43 (6), 767–784.

Wang, Fengwen, Lazarov, Boyan Stefanov, Sigmund, Ole, Jensen, Jakob Søndergaard, 2014. Interpolation scheme for fictitious domain techniques and topology optimization of finite strain elastic problems. Comput. Methods Appl. Mech. Engrg. 276, 453–472.

Wang, Liu, Zheng, Dongchang, Harker, Pablo, Patel, Aman B, Guo, Chuan Fei, Zhao, Xuanhe, 2021. Evolutionary design of magnetic soft continuum robots. Proc. Natl. Acad. Sci. 118 (21).

Wu, Shuai, Hamel, Craig M, Ze, Qiji, Yang, Fengyuan, Qi, H Jerry, Zhao, Ruike, 2020. Evolutionary algorithm-guided voxel-encoding printing of functional hard-magnetic soft active materials. Adv. Intell. Syst. 2 (8), 2000060.

Wu, Shuai, Ze, Qiji, Zhang, Rundong, Hu, Nan, Cheng, Yang, Yang, Fengyuan, Zhao, Ruike, 2019. Symmetry-breaking actuation mechanism for soft robotics and active metamaterials. ACS Appl. Mater. Interfaces 11 (44), 41649–41658.

Yan, Dong, Pezzulla, Matteo, Cruveiller, Lilian, Abbasi, Arefeh, Reis, Pedro M, 2020. Magneto-active elastic shells with tunable buckling strength. arXiv preprint arXiv:2012.01163.

Zhang, Xiaojia Shelly, Chi, Heng, Zhao, Zhi, 2021a. Topology optimization of hyperelastic structures with anisotropic fiber reinforcement under large deformations. Comput. Methods Appl. Mech. Engrg. 378, 113496.

Zhang, Shanshan, Li, Houmin, Huang, Yicang, 2021b. An improved multi-objective topology optimization model based on simp method for continuum structures including self-weight. Struct. Multidiscip. Optim. 63 (1), 211–230.

Zhang, Xiaojia, Ramos, Adeildo S., Paulino, Glaucio H., 2017. Material nonlinear topology optimization using the ground structure method with a discrete filtering scheme. Struct. Multidiscip. Optim. 55 (6), 2045–2072.

Zhang, Rundong, Wu, Shuai, Ze, Qiji, Zhao, Ruike, 2020. Micromechanics study on actuation efficiency of hard-magnetic soft active materials. J. Appl. Mech. 87 (9).

Zhao, Ruike, Kim, Yoonho, Chester, Shawn A, Sharma, Pradeep, Zhao, Xuanhe, 2019. Mechanics of hard-magnetic soft materials. J. Mech. Phys. Solids 124, 244–263.

Zhou, Yuqing, Nomura, Tsuyoshi, Saitou, Kazuhiro, 2018. Multi-component topology and material orientation design of composite structures (MTO-C). Comput. Methods Appl. Mech. Engrg. 342, 438–457.

Zhu, Benliang, Zhang, Xianmin, Zhang, Hongchuan, Liang, Junwen, Zang, Haoyan, Li, Hai, Wang, Rixin, 2020. Design of compliant mechanisms using continuum topology optimization: a review. Mech. Mach. Theory 143, 103622.